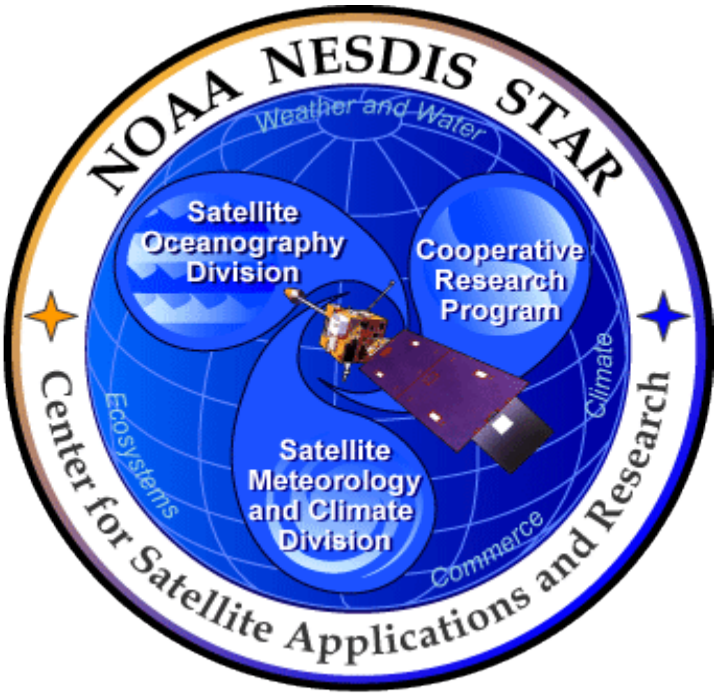

NOAA NESDIS
CENTER FOR SATELLITE APPLICATIONS AND RESEARCH

MODIS Ocean Color Products Using the SWIR Method

ALGORITHM THEORETICAL BASIS DOCUMENT

Version 1.0

THE MODIS-SWIR ALGORITHM THEORETICAL BASIS DOCUMENT VERSION 1.0

AUTHORS:

Menghua Wang (NOAA/NESDIS/STAR)

Xiaoming Liu (NOAA/NESDIS/STAR and SP Systems, Inc)

THE MODIS-SWIR ALGORITHM THEORETICAL BASIS DOCUMENT
VERSION HISTORY SUMMARY

Version	**Description**	**Revised Sections**	**Date**
1.0	New Document for MODIS-SWIR	New Document	02/17/2012

TABLE OF CONTENTS

LIST OF FIGURES

Page

LIST OF TABLES

Page

LIST OF ACRONYMS

ATBD	Algorithm Theoretical Basis Document
CDOM	Colored Dissolved Organic Material
CZCS	Coastal Zone Color Scanner
EOS	Earth Observing System
HAB	Harmful Algal Bloom
HDF	Hierarchical Data Format
IOCCG	The International Ocean-Colour Coordinating Group
JPSS	Joint Polar Satellite System
LUT	Lookup Table
MODIS	Moderate Resolution Imaging Spectroradiometer
NASA	National Aeronautics and Space Administration
NCDC	National Climate Data Center
NESDIS	National Environmental Satellite, Data, and Information Service
NGDC	National Geographic Data Center
NIR	Near Infrared
NOAA	National Oceanic and Atmospheric Administration
NOS	National Ocean Service
OSPO	Office of Satellite and Product Operations
PSDI	Product System Development and Implementation
R&D	Research & Development
SeaWiFS	Sea-viewing Wide Field-of-view Sensor
SNR	Signal to Noise Ratio
SSE	Single Scattering Epsilon
STAR	Center for Satellite Applications and Research
SWIR	Shortwave Infrared
TOA	Top of Atmosphere
UV	Ultraviolet
VIIRS	Visible Infrared Imaging Radiometer Suite

ABSTRACT

This document is the Algorithm Theoretical Basis Document (ATBD) for the MODIS ocean color products using the shortwave infrared (SWIR)-based atmospheric correction algorithm developed by the NOAA/NESDIS Center for Satellite Applications and Research (STAR). The MODIS ocean color processing algorithms include the atmospheric correction algorithm, and a suite of algorithms to generate ocean biological and biogeochemical products, such as chlorophyll-a concentration and the diffuse attenuation coefficient at the wavelength of 490 nm ($K_d(490)$). The main function of the atmospheric correction is to retrieve the normalized water-leaving radiance spectra $nL_w(\lambda)$ by removing the atmospheric and ocean surface effects from the satellite sensor-measured top-of-atmosphere (TOA) radiances. The current atmospheric correction algorithm was developed by *Gordon and Wang* (1994a), and has been used for SeaWiFS and MODIS, and has also been used for NOAA operational MODIS ocean color processing since 2006. However, the *Gordon and Wang* (1994a) algorithm was developed mainly for clear open ocean Case-I waters. To improve the data quality of the ocean color products in coastal productive and turbid waters, *Wang* (2007) proposed an atmospheric correction algorithm using the SWIR bands, and STAR was tasked to implement the SWIR-based atmospheric correction algorithm and ocean color data processing system into the current NOAA operational ocean color data processing system, OKEANOS. This document describes the details of the SWIR-based atmospheric correction algorithm and its implementation in ocean color data processing system.

1. INTRODUCTION

Ocean color is the water hue (water-leaving radiance spectra) due to the presence of tiny plants and particles containing the pigment chlorophyll, sediments, and colored dissolved organic material (CDOM). Ocean color satellite remote sensing was started with the Coastal Zone Color Scanner (CZCS) (*Gordon et al.*, 1980; *Hovis et al.*, 1980) as a proof-of-concept mission in which it demonstrated the feasibility of quantitative retrieval of the ocean near-surface bio-optical data. After the CZCS mission, a number of follow-on satellite instruments that are capable of ocean color measurements have been launched. Particularly, with the successful flight of the Sea-viewing Wide Field-of-view Sensor (SeaWiFS) (*Hooker et al.*, 1992; *McClain et al.*, 2004) (1997–2010) and the Moderate Resolution Imaging Spectroradiometer (MODIS) (*Esaias et al.*, 1998; *Salomonson et al.*, 1989) on the Earth Observing System's Terra (December 1999–present) and Aqua (May 2002–present), we now have an unprecedented view of chlorophyll patterns on global scales by using the advanced data processing (*McClain*, 2009). The global ocean color data have been used by researchers and scientists worldwide to study and understand ocean physical, optical, biological, and biogeochemical changes and their effects on the climate, e.g., (*Behrenfeld et al.*, 2006; *Behrenfeld et al.*, 2001; *Chavez et al.*, 1999; *Siegel et al.*, 2002). The Visible Infrared Imaging Radiometer Suite (VIIRS) on board of the Suomi National Polar-orbiting Partnership (Suomi NPP), which was successfully launched in October of 2011, will continue to provide global ocean color products, with the operational platforms from the Joint Polar Satellite System (JPSS) to follow sometime later. Table 1 provides characteristics of the ocean color spectral bands for VIIRS, MODIS, and SeaWiFS. In addition, spectral bands that are designed for the atmosphere and land applications, e.g., the shortwave infrared (SWIR) bands, but can also be useful for the ocean color application in the coastal regions are listed in Table 1 (for both MODIS and VIIRS). It is noted that MODIS and VIIRS have similar ocean color and SWIR spectral bands. Algorithms developed in MODIS can generally be applied also to VIIRS.

Satellite ocean color products are important for ocean environment monitoring and forecast. For examples, chlorophyll-a (Chl-a) concentration (*O'Reilly et al.*, 1998) provides an estimate of the live phytoplankton biomass in the ocean surface layer, and the water diffuse attenuation coefficient at the wavelength of 490 nm (K_d(490)) (*Lee et al.*, 2002; *Morel et al.*, 2007; *Mueller*, 2000; *Wang et al.*, 2009a) indicates the turbidity of the water column. K_d(490) is an important water property related to light penetration and availability in aquatic systems. Accurate estimation of the diffuse attenuation coefficient is critical to understand not only physical processes such as the heat transfer in the upper layer of the ocean (*Lewis et al.*, 1990; *Morel and Antoine*, 1994; *Sathyendranath et al.*, 1991; *Wu et al.*, 2007), but also biological processes such as phytoplankton photosynthesis in the ocean euphotic zone (*Platt et al.*, 1988; *Sathyendranath et al.*, 1989). These ocean biological and biogeochemical parameters are all derived from satellite-measured normalized water-leaving radiance spectra $nL_w(\lambda)$ (*Gordon and Wang*, 1994a; *IOCCG*, 2010). Ocean color products derived from MODIS-Aqua have been generated operationally at the NOAA Office of Satellite and Product Operations (OSPO) since 2006, and used for Gulf of Mexico Harmful Algal Bloom (HAB) bulletin by National Ocean Service (NOS) to provide notification of bloom conditions to state and local coastal managers in the Gulf of Mexico.

TABLE 1. The ocean color and other useful spectral bands for VIIRS, MODIS, SeaWiFS.

VIIRS		MODIS		SeaWiFS
Ocean Bands (nm)	Other Bands (nm)	Ocean Bands (nm)	Other Bands (nm)	Ocean Band (nm)
412		412	645	412
445		443	859	443
488		488	469	490
—		531	555	510
555	*SWIR Bands*	551	*SWIR Bands*	555
672	1240	667	1240	670
746	1610	748	1640	765
865	2250	869	2130	865

1.1. Purpose

There are mainly two stages in the satellite ocean color data processing from the calibrated and geolocated radiances (Level-1B) to the derived geophysical products (Level-2): (1) apply the atmospheric correction algorithm to generate normalized water-leaving radiance spectra $nL_w(\lambda)$ and (2) generate a suite of ocean color products such as chlorophyll-a concentration and $K_d(490)$ using the $nL_w(\lambda)$ data obtained in the first stage.

Atmospheric correction algorithm is a key procedure in the satellite ocean color data processing. The main function of the atmospheric correction is to retrieve the normalized water-leaving radiance spectra $nL_w(\lambda)$ from the satellite-measured TOA radiances by removing the atmospheric and ocean surface effects (*Antoine and Morel*, 1999; *Fukushima et al.*, 1998; *Gordon and Wang*, 1994a; *IOCCG*, 2010). The atmospheric correction algorithm used in the current operational MODIS ocean color data processing at OSPO was based on the *Gordon and Wang* (1994a). In the *Gordon and Wang* (1994a) algorithm, the aerosol reflectance is estimated using two near-infrared (NIR) bands at 748 and 869 nm with the assumption of the black ocean at these two NIR wavelengths. The NIR black ocean assumption is usually valid at the open oceans with generally low chlorophyll-a concentration. However, for highly productive ocean waters and turbid waters in the coastal regions, the ocean contributions in the NIR bands are no longer negligible and can be very significant. In these cases, atmospheric correction often results in significant errors (*Lavender et al.*, 2005; *Ruddick et al.*, 2000; *Siegel et al.*, 2000; *Wang and Shi*, 2005). In fact, some modifications have been made to account for the NIR ocean radiance contributions for non-highly turbid waters (*Bailey et al.*, 2010; *Stumpf et al.*, 2003).

For dealing with the turbid waters in coastal regions, *Wang* (2007) proposed an atmospheric correction algorithm using the SWIR bands. At the SWIR wavelengths, ocean water has much stronger absorption than that at the NIR bands (*Hale and Querry*, 1973; *Kou et al.*, 1993), thus the black ocean assumption is generally valid at the SWIR bands, even for very turbid water (*Shi and Wang*, 2009c). Furthermore, to address the noise issue for the MODIS SWIR bands (*Wang*,

2007; *Wang and Shi*, 2012; *Werdell et al.*, 2010), *Wang and Shi* (2007) proposed a method of ocean color data processing using the combined NIR and SWIR bands for atmospheric correction for MODIS. With the proposed NIR-SWIR combined atmospheric correction algorithm, MODIS ocean color data can be processed using the standard-NIR atmospheric correction algorithm for the open oceans, whereas for the turbid waters in the coastal region the SWIR atmospheric correction algorithm can be executed (*Wang and Shi*, 2007). Based on these findings, a new project was proposed and funded by the NOAA/NESDIS Product System Development and Implementation (PSDI) program for developing a new operational MODIS ocean color products using the SWIR-based atmospheric correction algorithm, and implement it in the operational ocean color data processing system at OSPO, OKEANOS.

The algorithm for calculating ocean chlorophyll-a concentration (*O'Reilly, et al.*, 1998; *O'Reilly et al.*, 2000) from the normalized water-leaving radiance spectra $nL_w(\lambda)$ has not been changed in this new project. However, a new algorithm is proposed for the ocean color product $K_d(490)$ (*Wang, et al.*, 2009a). Therefore, this document will mainly focus on the descriptions of the SWIR-based atmospheric correction algorithm and the new $K_d(490)$ algorithm for producing ocean color products operationally.

1.2. Scope

This document will describe the SWIR-based algorithm (specifically the combined NIR-SWIR atmospheric correction algorithm), which is proposed to process MODIS ocean color data from the calibrated and geolocated radiances (Level-1B) to the derived geophysical products (Level-2). Since the proposed algorithm differ from the current operational MODIS ocean color algorithm mainly in the atmosphere correction algorithm, this document will focus on the atmophere correction algorithm.

2. ALGORITHM DESCRIPTION

2.1. Data Processing Outline

The MODIS-NIR-SWIR ocean color data processing system processes MODIS-Aqua 5-minute granule data from Level-1B to Level-2 in the CoastWatch regions daily. The data processing procedure includes the following steps:

Step 1: Read the input parameter file, Level-1B file, geolocation file, ancillary data, and required lookup tables.
Step 2: Make corrections of ozone and water vapor absorptions to the sensor-measured TOA radiances. Calculate ozone, water vapor, whitecap, sun glint, and polarization corrections.
Step 3: Compute Rayleigh scattering radiances, whitecap radiances, and sun glint masking and correction (if it is needed).
Step 4: Calculate the spectral aerosol radiance contributions.
Step 5: Compute atmospheric diffuse attenuation coefficients for solar- and sensor-zenith angles.
Step 6: Remove aerosol spectral radiance contributions to derive water-leaving radiance spectra, and calculate normalized water-leaving radiance spectra $nL_w(\lambda)$.
Step 7: Calculate the required ocean color products, including $nL_w(\lambda)$, chlorophyll-a, and $K_d(490)$, etc.
Step 8: Write out the ocean color product data into the Level-2 output file.

2.2. Algorithm Input

2.2.1. MODIS Data

The ocean color data processing takes the calibrated TOA radiances at the following wavelengths in the MODIS Level-1B file: 412, 443, 469, 488, 531, 551, 555, 645, 667, 678, 748, 859, 869, 1240, and 2130 nm. In addition, the algorithm also needs the geolocation information such as solar-zenith angle, sensor-zenith angle, and relative azimuth angle, as well as latitude and longitude from the MODIS geolocation file.

2.2.2. Ancillary Data

The NIR-SWIR ocean color data processing also takes the following ancillary data as inputs (*Ramachandran and Wang*, 2011):
(a) Ozone concentration: the input is required for the correction of ozone absorption in the sensor-measured TOA radiances.
(b) Surface atmosphere pressure: the input is required to compute the spectral Rayleigh radiances.
(c) Surface wind speed: the input is required to calculate the spectral Rayleigh radiances, whitecap radiances, and sun glint radiance contributions.
(d) Water vapor amount: the input is required for the correction of water vapor absorption in the sensor-measured radiances at the NIR and SWIR bands.

2.3. Theoretical description of the NIR-SWIR-based atmospheric correction algorithm

The proposed NIR-SWIR ocean color data processing is an enhancement of the current operational ocean color data processing system that uses the NIR-based atmosphere correction algorithm. In this section, we will describe the current operational NIR-based algorithm in Section 2.3.1 and the SWIR-based algorithm proposed by *Wang* (2007) in Section 2.3.2. The NIR-SWIR-based algorithm proposed by *Wang and Shi* (2007) will be described in Section 2.3.3. At last, the new $K_d(490)$ algorithm will also be briefly described in Section 2.3.4.

2.3.1. NIR-based atmospheric correction algorithm

Briefly, by defining the reflectance $\rho(\lambda) = \pi L(\lambda)/[\cos\theta_0 F_0(\lambda)]$, where $L(\lambda)$ is the upward radiance in the given viewing direction, $F_0(\lambda)$ is the extraterrestrial solar irradiance, and θ_0 is the solar-zenith angle, the total upwelling reflectance at the top of atmosphere (TOA), measured at a wavelength λ, can be written as:

$$\rho_t(\lambda) = \rho_r(\lambda) + \rho_A(\lambda) + T(\lambda)\rho_g(\lambda) + t(\lambda)\rho_{wc}(\lambda) + t(\lambda)\rho_w(\lambda), \quad (1)$$

where $\rho_r(\lambda)$ and $\rho_A(\lambda)$ are the reflectance contributions from multiple scattering of molecules (Rayleigh scattering) (*Gordon et al.*, 1988; *Gordon and Wang*, 1992; *Wang*, 2005) and aerosols (including Rayleigh-aerosol interactions) (*Deschamps et al.*, 1983; *Gordon and Wang*, 1994a; *IOCCG*, 2010), respectively. $\rho_g(\lambda)$ is the sun glint radiance (*Wang and Bailey*, 2001), $\rho_{wc}(\lambda)$ is the reflectance from whitecaps (*Frouin et al.*, 1996; *Gordon and Wang*, 1994b; *Moore et al.*, 2000), and $\rho_w(\lambda)$ is the water-leaving reflectance which is desired quantity in the ocean color remote sensing. $T(\lambda)$ and $t(\lambda)$ are, at the sensor viewing direction, the atmospheric direct and diffuse transmittance (*Wang*, 1999b; *Yang and Gordon*, 1997), respectively. The objective of the atmospheric correction is to retrieve the water-leaving reflectance $\rho_w(\lambda)$ accurately from the sensor-measured reflectance spectral $\rho_t(\lambda)$.

The normalized water-leaving reflectance $\rho_{wN}(\lambda)$ is defined as (to remove the atmospheric effects in $\rho_w(\lambda)$):

$$\rho_{wN}(\lambda) = \rho_w(\lambda) / t(\lambda, \theta_0), \quad (2)$$

where $t(\lambda,\theta_0)$ is atmospheric diffuse transmittance in the solar direction. It is also common to use the normalized water-leaving radiance $nL_w(\lambda)$ and remote-sensing reflectance $R_{rs}(\lambda)$. They are related to $\rho_{wN}(\lambda)$ as:

$$nL_w(\lambda) = \frac{F_0(\lambda)}{\pi}\rho_{wN}(\lambda), \; R_{rs}(\lambda) = \frac{1}{\pi}\rho_{wN}(\lambda). \quad (3)$$

The function of atmosphere correction is to retrieve normalized water-leaving reflectance $\rho_{wN}(\lambda)$ from the total reflectance measured at the satellite sensor, i.e., deriving $\rho_{wN}(\lambda)$ from sensor-measured $\rho_t(\lambda)$ in Eq. (1). However, the radiance backscattered from the atmosphere and/or sea surface is typically an order of magnitude larger than the desired radiance scattered

out of the water (*IOCCG*, 2010), thus the atmosphere and sea surface effects need to be accurately removed from the sensor-measured TOA radiance. Removing a large signal and keeping a very small signal from the water is a major challenge of the atmospheric correction over the ocean (*IOCCG*, 2010).

Removing the sun glint (*Wang and Bailey*, 2001) and whitecap (*Gordon and Wang*, 1994b) reflectance contributions from the TOA reflectance is straightforward. Sun glint is originated from specular reflection of direct sunlight by the sea surface (sun glitter) (*Cox and Munk*, 1954; *Zhang and Wang*, 2010). Significant sun glint contributions with certain viewing geometries are mostly masked out, and the residual glint contamination is corrected based on a model of sea surface slope distribution (*Cox and Munk*, 1954; *Wang and Bailey*, 2001). Ocean whitecap reflectance is originated from reflection of direct sunlight and skylight from ocean whitecaps. The whitecap reflectance contribution for each band is generally small (*Moore, et al.*, 2000) and is calculated as a function of sea surface wind speed and viewing geometry (*Frouin, et al.*, 1996; *Gordon and Wang*, 1994b; *Moore, et al.*, 2000). These algorithms have not been changed in the new proposed SWIR and NIR-SWIR atmospheric correction algorithms.

We can further define the atmospheric path reflectance $\rho_{path}(\lambda)$, which is originated along the optical path from scattering in the atmosphere and from specular reflection of scattered light (skylight) by the sea surface, and it can be decomposed into two components:

$$\rho_{path}(\lambda) = \rho_r(\lambda) + \rho_A(\lambda), \tag{4}$$

where $\rho_r(\lambda)$ is the Rayleigh reflectance from multiple scattering by air molecules (*Gordon, et al.*, 1988; *Gordon and Wang*, 1992; *Wang*, 2005), and $\rho_A(\lambda)$ is the aerosol reflectance (including Rayleigh-aerosol interactions) from multiple scattering by particles (*Deschamps, et al.*, 1983; *Gordon and Wang*, 1994a; *IOCCG*, 2010). The Rayleigh radiance, $\rho_r(\lambda)$, can be computed accurately from the Raleigh lookup tables that were generated using the vector radiative transfer theory (including polarization) with inputs of the solar-sensor geometry, atmospheric pressure, and wind speed (*Gordon, et al.*, 1988; *Gordon and Wang*, 1992; *Wang*, 2002, 2005). The major challenge of the atmosphere correction is to estimate and remove the aerosol reflectance, $\rho_A(\lambda)$, from the TOA reflectance.

With the assumption that water-leaving reflectances are negligible in the NIR bands (748 and 869 nm) in the open ocean, the aerosol reflectance, $\rho_A(\lambda)$, can be estimated by removing Rayleigh reflectance, sun glint, and whitecap reflectance from the TOA reflectance in the two NIR bands. The aerosol models are used to estimate the aerosol reflectance contributions in visible bands, through using aerosol lookup tables. The aerosol lookup tables were also generated using the vector radiative transfer theory with including polarization effects (*Wang*, 2006). The algorithm selects from a family of 12 aerosol models to fit the aerosol radiance contributions in the NIR bands, and the selected models are then used to extrapolate the aerosol radiances from the NIR to visible bands (*Gordon and Wang*, 1994a; *Wang*, 1999a, 2004, 2007).

The 12 aerosol models derived from the work of *Shettle and Fenn* (1979) are used in the MODIS data processing. Specifically, they are the oceanic model with relative humidity of 99% (O99), the maritime models with relative humidity of 50%, 70%, 90%, 99% (M50, M70, M90, M99), the coastal models with relative humidity of 50%, 70%, 90%, 99%, (C50, C70, C90, C99),

and the tropospheric models with relative humidity of 50%, 90%, 99% (T50, T90, T99) (*Gordon and Wang*, 1994a; *Shettle and Fenn*, 1979; *Wang*, 1999a). These aerosol models are used to generate lookup tables (LUTs) for computing $\rho_A(\lambda)$. Briefly, for each aerosol model radiative transfer, computations are carried out to determine $\rho_{path}(\lambda)$ as a function of the aerosol optical thickness for a variety of solar-sensor geometries. The computations use complete vector radiative transfer, i.e., including polarization effects (*Wang*, 2006). The appropriate $\rho_r(\lambda)$ is then subtracted from the $\rho_{path}(\lambda)$ yielding $\rho_A(\lambda)$, which is then fit to a fourth order polynomial in the single-scattered aerosol reflectance for a given geometry (*Wang*, 2006, 2007). The LUTs contain the fitting coefficients for a large number of viewing-sun geometries and for values of the aerosol optical thickness up to 0.8 (see details in next section).

The procedure for estimating $\rho_A(\lambda)$ in visible bands is to estimate this quantity in the NIR bands first, assuming negligible water-leaving radiance in that region of the spectrum for the open oceans. Using the aerosol LUTs, the sensor-measured spectral variation of $\rho_A(\lambda)$ at the two NIR bands can be used to estimate the single-scattered aerosol reflectance $\rho_{as}(\lambda)$ (*Gordon and Wang*, 1994a; *Wang*, 2004; *Wang and Gordon*, 1994) for the same two bands. As $\rho_{as}(\lambda)$ is related directly to the aerosol phase function, single scattering albedo, and optical thickness, it can be computed directly for each aerosol model. It is then possible to select the most appropriate aerosol models for which the computed radiances are best matched with the measured values. This is accomplished by comparing the measured value of the single scattering epsilon (SSE) with those computed for each model (*Gordon and Wang*, 1994a; *Wang*, 2004; *Wang and Gordon*, 1994). This approach is used because the SSE depends only on the aerosol model, and not on the aerosol optical thickness. Based on the derived SSE values in the NIR bands, the two most appropriate aerosol models (from the set of 12 models) are retrieved and used for estimation of the aerosol effects in the visible bands, $\rho_{as}(\lambda)$ and $\rho_A(\lambda)$. Therefore, the water-leaving radiance (reflectance) in the visible wavelengths can then be derived. Results show that the *Shettle and Fenn* (1979) aerosol models are sufficient to derive accurate normalized water-leaving reflectance (radiance) spectra, compared with results from using more updated aerosol models for atmospheric correction (*Ahmad et al.*, 2010).

2.3.2. SWIR-based atmospheric correction algorithm and its implementation

In the NIR-based atmospheric correction algorithm as described in Section 2.3.1, the aerosol reflectances are calculated with assumption of the black ocean in the two NIR bands, i.e., there are no ocean radiance contributions at the NIR bands. The NIR black ocean assumption is usually valid at the open oceans where the ocean optical properties are mainly as a function of the pigment concentration with generally low pigment concentration value. However, for highly productive ocean waters and for turbid waters in the coastal regions (e.g., waters with high sediment concentration), the water-leaving radiances in NIR bands are no longer negligible and can be very significant (*Lavender, et al.*, 2005; *Ruddick, et al.*, 2000; *Siegel, et al.*, 2000; *Stumpf, et al.*, 2003; *Wang and Shi*, 2005). In these cases, atmospheric correction often results in significant error in the derived water-leaving radiances in the visible bands. This is basically

because at the NIR wavelengths water absorptions are not large enough to absorb photons backscattered by particles from the oceans.

Wang (2007) proposed and evaluated a new atmospheric correction algorithm, which uses SWIR bands to derive the normalized water-leaving reflectance spectra from the UV to the visible and NIR wavelengths. For wavelengths longer than the NIR band, water absorption increases very rapidly as the increase of wavelength. Indeed, for the SWIR wavelengths (> ~1000 nm), water has much stronger absorption than that at 865 nm. Specifically, from *Hale and Querry* (1973), the water absorption coefficients for wavelengths at 865, 1000, 1240, 1640, and 2130 nm are about 5, 36, 88, 498, and 2228 m^{-1}, respectively. Therefore, with the black ocean assumption, the SWIR bands can be used for detecting turbid waters (*Shi and Wang*, 2007b), as well as for atmospheric correction in the coastal ocean regions (*Wang*, 2007; *Wang and Shi*, 2007; *Wang et al.*, 2009b).

Using the same 12 aerosol models as described in Section 3.2.1, *Wang* (2007) generated the aerosol optical property data for spectral bands at UV (340 nm) and SWIR (1000, 1240, 1640, and 2130 nm) wavelengths in addition to other MODIS spectral bands at 412, 443, 469, 488, 531, 551, 555, 645, 667, 678, 748, 859 and 869 nm. Similar to the generation of the MODIS ocean band aerosol lookup tables, the aerosol lookup tables for the UV and SWIR bands were generated using the vector radiative transfer simulations (including polarization) (*Wang*, 2006) that were carried out with the 12 aerosol models for nine aerosol optical thicknesses (0.02, 0.05, 0.1, 0.15, 0.2, 0.3, 0.4, 0.6, and 0.8), 33 solar-zenith angles from 0°–80° at a step of 2.5°, and 35 sensor-zenith angles from 1°–75° at a step of ~2°. The aerosol SSE parameter $\varepsilon(\lambda, \lambda_0)$ is defined as the ratio of the aerosol single-scattering reflectance $\rho_{as}(\lambda)$ between two bands, i.e.,

$$\varepsilon(\lambda,\lambda_0)=\frac{\rho_{as}(\lambda)}{\rho_{as}(\lambda_0)}\equiv\frac{\omega_a(\lambda)c_{ext}(\lambda)p_a(\theta_0,\theta,\Delta\phi,\lambda)}{\omega_a(\lambda_0)c_{ext}(\lambda_0)p_a(\theta_0,\theta,\Delta\phi,\lambda_0)}, \quad (5)$$

where $\omega_a(\lambda)$, $c_{ext}(\lambda)$, and $p_a(\theta, \theta_0, \Delta\phi, \lambda)$ are the aerosol single-scattering albedo, the aerosol extinction coefficient, and the aerosol effective scattering phase function, respectively. The SSE depends mainly on the aerosol model and can be used to characterize the aerosol spectral variation for various aerosol models. Figure 1 provides examples of the SSE as a function of the wavelength (from the UV to NIR or to various SWIR bands) for the 12 aerosol models. Figures 1(a)-1(d) show the SSE $\varepsilon(\lambda, \lambda_0)$ at the reference wavelengths λ_0 of 865, 1240, 1640, and 2130 nm, respectively. They are all for the case of a solar-zenith angle of 60°, sensor-zenith angle of 20°, and relative-azimuth angle of 90°. As expected, the $\varepsilon(\lambda, \lambda_0)$ value has significant variations corresponding to various reference wavelength λ_0 values. Between the O99 and the T50 models (from the lowest to the highest SSE values), Fig. 1 shows that the SSE values at the UV band for ε(340, 865), ε(340, 1240), ε(340, 1640), and ε(340, 2130) are in the range of 0.8–2.6, 0.7–4.8, 0.7–9.2, and 0.7–22.6, respectively. Particularly, the NIR and SWIR SSE values of ε(765, 865), ε(1000, 1240), ε(1240, 1640), ε(1240, 2130), and ε(1640, 2130), which are used for the selection of aerosol models in atmospheric correction, are in the range of 0.96–1.21, 0.93–1.50, 0.95–1.94, 0.98–4.76, and 1.04–2.46, respectively. Obviously, there are significantly higher measurement

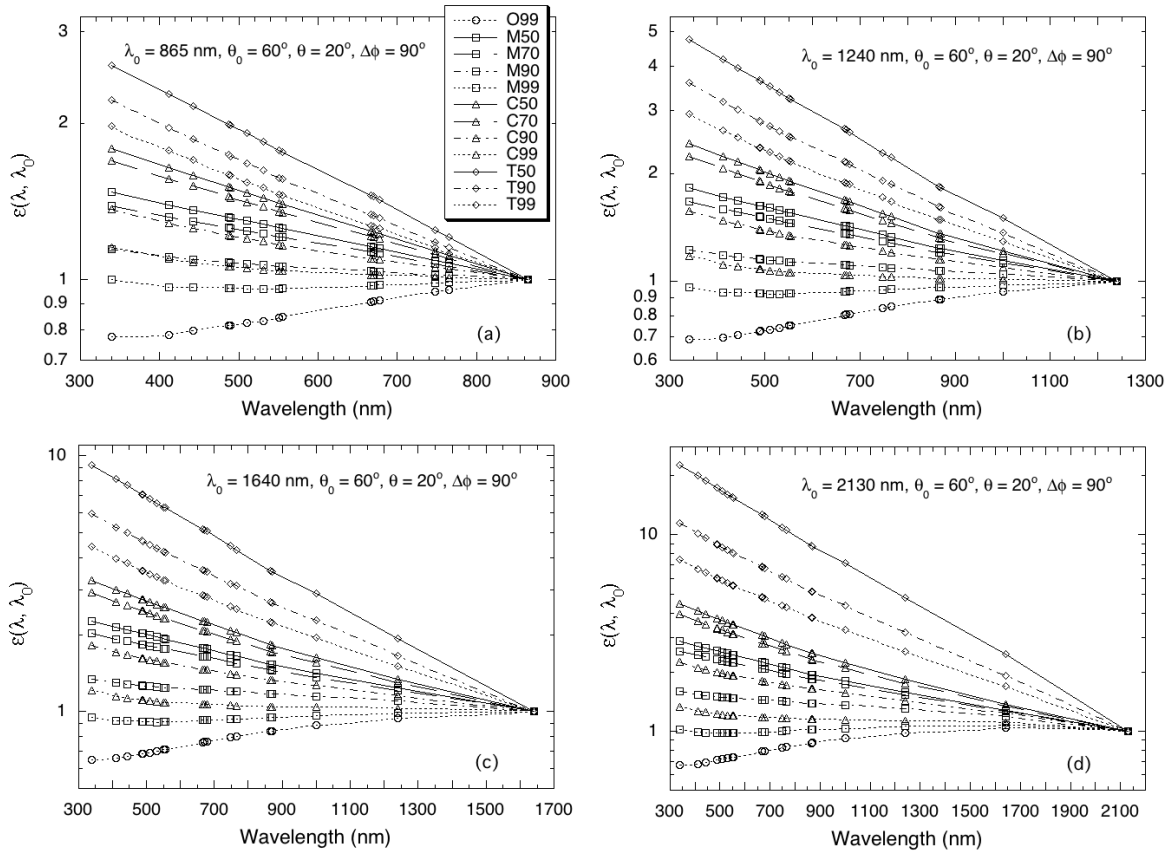

Figure 1. Single-scattering epsilon as a function of the wavelength for the 12 aerosol models and for the reference wavelength at (a) 865 nm, (b) 1240 nm, (c) 1640 nm, and (d) 2130 nm (Wang, 2007).

sensitivities in the SSE with the SWIR bands where there is a substantially larger apart of wavelength distance between two bands, e.g., $\varepsilon(1240, 2130)$.

The implementation of the aerosol lookup tables into the data processing system can be achieved by relating the aerosol reflectance $\rho_A(\lambda)$ to its corresponding single-scattering aerosol reflectance $\rho_{as}(\lambda)$, i.e.,

$$\rho_A\left(\lambda_j,\theta_0,\theta,\Delta\phi,\tau_a\right)=\sum_{i=0}^{4} a_i\left(\lambda_j,\theta_0,\theta,\Delta\phi\right)\left[\rho_{as}\left(\lambda_j,\theta_0,\theta,\Delta\phi,\tau_a\right)\right]^i, \quad (6)$$

where $a_i(\lambda_j,\theta_0,\theta,\Delta\phi)$ are coefficients to fit 4th power polynomial for $\rho_A(\lambda_j,\theta_0,\theta,\Delta\phi,\tau_a)$ as a function of $\rho_{as}(\lambda_j,\theta_0,\theta,\Delta\phi,\tau_a)$ in the least-square for all spectral bands λ_j from the UV to the SWIR and for the solar-zenith angle θ_0 from 0°–80° at every 2.5°, the sensor-zenith angle θ from 1°–75° at every ~2°, and the relative-azimuth angle $\Delta\phi$ from 0°–180° at every of 10°. Coefficients

$a_i(\lambda_j,\theta_0,\theta,\Delta\phi)$ were derived by fitting the curves that were obtained from data simulated with aerosol optical thicknesses $\tau_a(\lambda)$ of 0.02, 0.05, 0.1, 0.15, 0.2, 0.3, 0.4, 0.6, and 0.8 for the 12 aerosol models. On the other hand, the sensor-measured NIR or SWIR aerosol reflectances need to be converted to the aerosol single-scattering reflectance for atmospheric correction as well as for retrieval of aerosol optical properties. Therefore, coefficients were also generated for computing the aerosol single-scattering reflectance $\rho_{as}(\lambda)$ as a function of the aerosol reflectance $\rho_A(\lambda)$ at the NIR and SWIR bands, i.e.,

$$\rho_{as}\left(\lambda_j,\theta_0,\theta,\Delta\phi,\tau_a\right)=\sum_{i=0}^{4} b_i\left(\lambda_j,\theta_0,\theta,\Delta\phi\right)\left[\rho_A\left(\lambda_j,\theta_0,\theta,\Delta\phi,\tau_a\right)\right]^i, \quad (7)$$

where $b_i(\lambda_j,\theta_0,\theta,\Delta\phi)$ are coefficients to fit 4th power polynomial for $\rho_{as}(\lambda_j,\theta_0,\theta,\Delta\phi,\tau_a)$ as a function of $\rho_A(\lambda_j,\theta_0,\theta,\Delta\phi,\tau_a)$ in the least-square for the NIR and SWIR bands, i.e., 765, 865, 1000, 1240, 1640, and 2130 nm. By directly calculating $\rho_{as}(\lambda_j,\theta_0,\theta,\Delta\phi,\tau_a)$ using Eq. (7) instead of solving Eq. (6), it eliminates uncertainty and increases computing efficiency in numerical solution for the high order polynomials (Eq. (6)). These methods (Eqs. (6) and (7)) are accurate and efficient in the data processing. Therefore, the aerosol lookup tables are generated as in the forms with which coefficients $a_i(\lambda_j,\theta_0,\theta,\Delta\phi)$ (for all spectral bands from the UV to the SWIR) and $b_i(\lambda_j,\theta_0,\theta,\Delta\phi)$ (for the NIR and SWIR bands) are stored for the solar-zenith angles from 0°–80° at a step of 2.5°, the sensor-zenith angles from 1°–75° at a step of ~2°, and the relative-azimuth angles from 0°–180° at a step of 10°. For any given solar-sensor geometry, a linear interpolation (3-dimension) is carried out to produce the corresponding coefficients $a_i(\lambda_j,\theta_0,\theta,\Delta\phi)$ and $b_i(\lambda_j,\theta_0,\theta,\Delta\phi)$ for computations of $\rho_A(\lambda_j,\theta_0,\theta,\Delta\phi,\tau_a)$ at the UV to the SWIR bands and $\rho_{as}(\lambda_j,\theta_0,\theta,\Delta\phi,\tau_a)$ at the NIR or SWIR bands.

It is noted that, specifically to the MODIS-Aqua data processing, aerosol lookup tables were generated and implemented for 16 MODIS spectral bands at 412, 443, 469, 488, 531, 551, 555, 645, 667, 678, 748, 859, 869, 1240, 1640, and 2130 nm.

To understand the algorithm performance in retrieval of the water-leaving reflectance spectra using various combinations of the SWIR bands, simulations have been carried out using the pseudo TOA reflectance simulated with the M80 and the T80 aerosol models as inputs. The outputs from the atmospheric correction algorithm using various combinations of the SWIR bands are compared with results that are derived from the NIR-based algorithm. Figures 2 and 3 provide examples of the error in the retrieved water-leaving reflectance from method performed using various combinations of the NIR and SWIR bands. Figures 2(a)–2(d) are the error in the derived water-leaving reflectance $[t\rho_w(\lambda)]$, for the M80 model with $\tau_a(865)$ of 0.1, as a function of the solar-zenith angle for algorithm performed using bands of 765 and 865 nm, 1240 and 1640 nm, 1240 and 2130 nm, and 1640 and 2130 nm, respectively, while Figures 3(a)–3(d) are the corresponding results for the T80 aerosol model. These are all for a case of the sensor-zenith angle of 45° and the relative-azimuth angle of 90°. Results in Fig. 2 show that, for the M80 model, the atmospheric correction performed using the SWIR band combinations of 1000 and 1240 nm, 1240 and 1640 nm, and 1240 and 2130 nm has comparable results as from algorithm

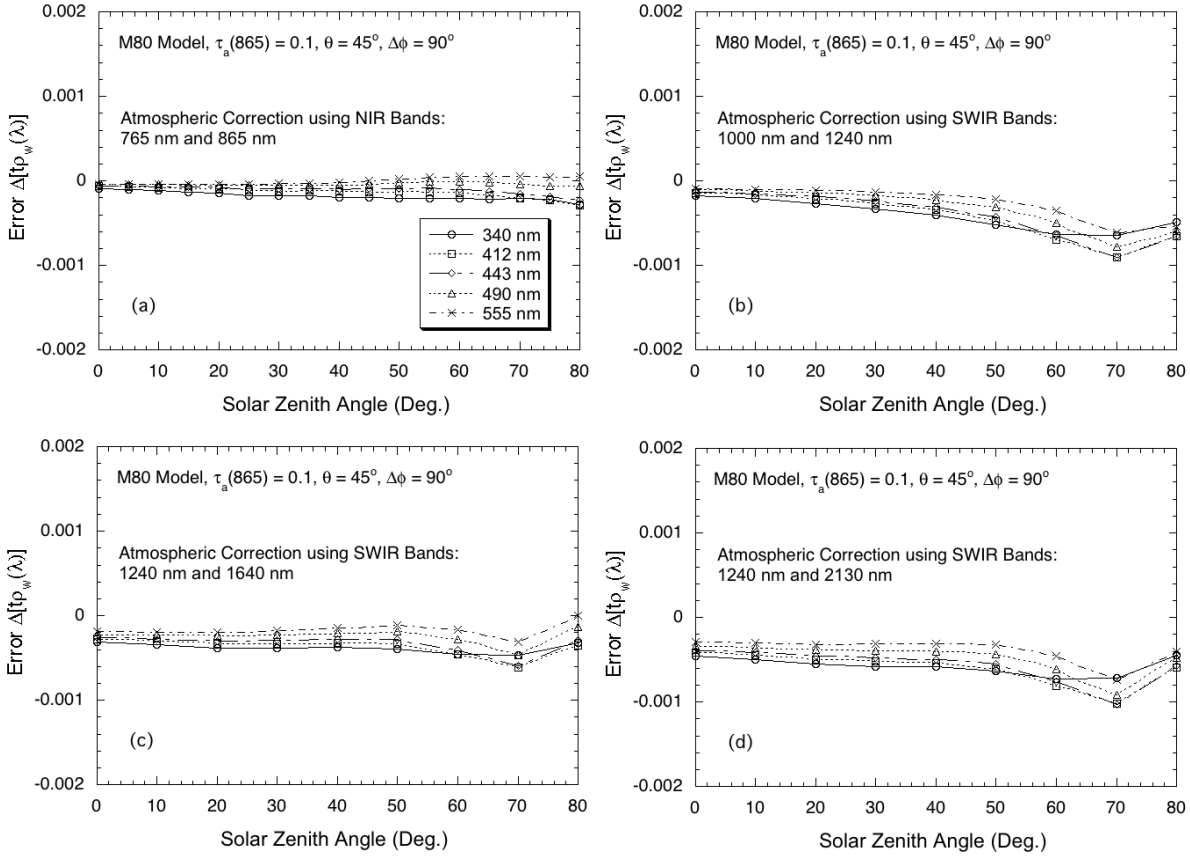

Figure 2. Error in the derived water-leaving reflectance at wavelengths 340, 412, 443, 490, and 555 nm as a function of the solar-zenith angle for the M80 aerosol model with of 0.1 and for algorithm performed using band combinations of (a) 765 and 865 nm, (b) 1000 and 1240 nm, (c) 1240 and 1640, and (d) 1240 and 2130 nm. This is for the case of sensor-zenith angle of 45° and relative-azimuth angle of 90° (Wang, 2007)

using the two NIR (765 and 865 nm) bands. Errors in the derived $[t\rho_w(\lambda)]$ are all within 0.001 (usually within ~0.0005) for the UV (340 nm) and visible wavelengths (412, 443, 490, and 555 nm). We can draw similar conclusions for the T80 model for cases with which the solar-zenith angles ≤ 70° (Fig. 3).

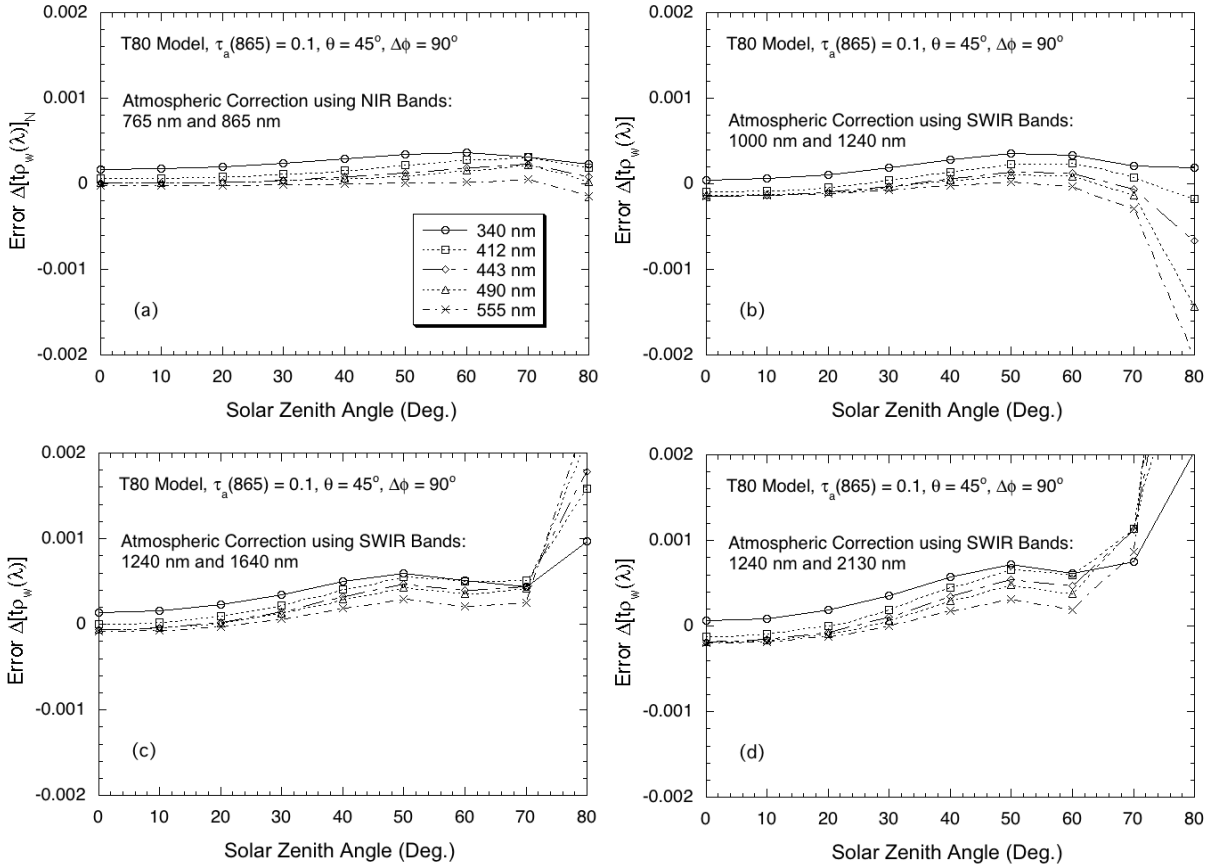

Figure 3. Same as in Fig. 2 except that they are for the T80 aerosol model (*Wang*, 2007).

Using combinations of the SWIR bands for atmospheric correction, the water-leaving reflectances at the NIR bands can also be derived. Figure 4 gives examples of the accuracy in the derived water-leaving reflectances $\Delta[t\rho_w(\lambda)]$ at the NIR bands for the M80 and the T80 aerosol models with $\tau_a(865)$ of 0.1. Figures 4(a) and 4(b) are errors in the derived water-leaving reflectance $\Delta[t\rho_w(\lambda)]$ for the M80 aerosols as a function of the solar-zenith angle for wavelengths at 765 and 865 nm, respectively, while Figs. 4(c) and 4(d) are results in $\Delta[t\rho_w(\lambda)]$ for the T80 model for wavelengths at 765 and 865 nm, respectively. In addition to the three combinations of the SWIR bands presented in Figs. 2 and 3, method using the SWIR bands of 1640 and 2130 nm has also been included in Fig. 4. Results in Fig. 4 show that, except for the method using 1640 and 2130 nm, errors $\Delta[t\rho_w(\lambda)]$ are almost all within uncertainty of ~10^{-4} for cases with which the solar-zenith angles ≤ 70°.

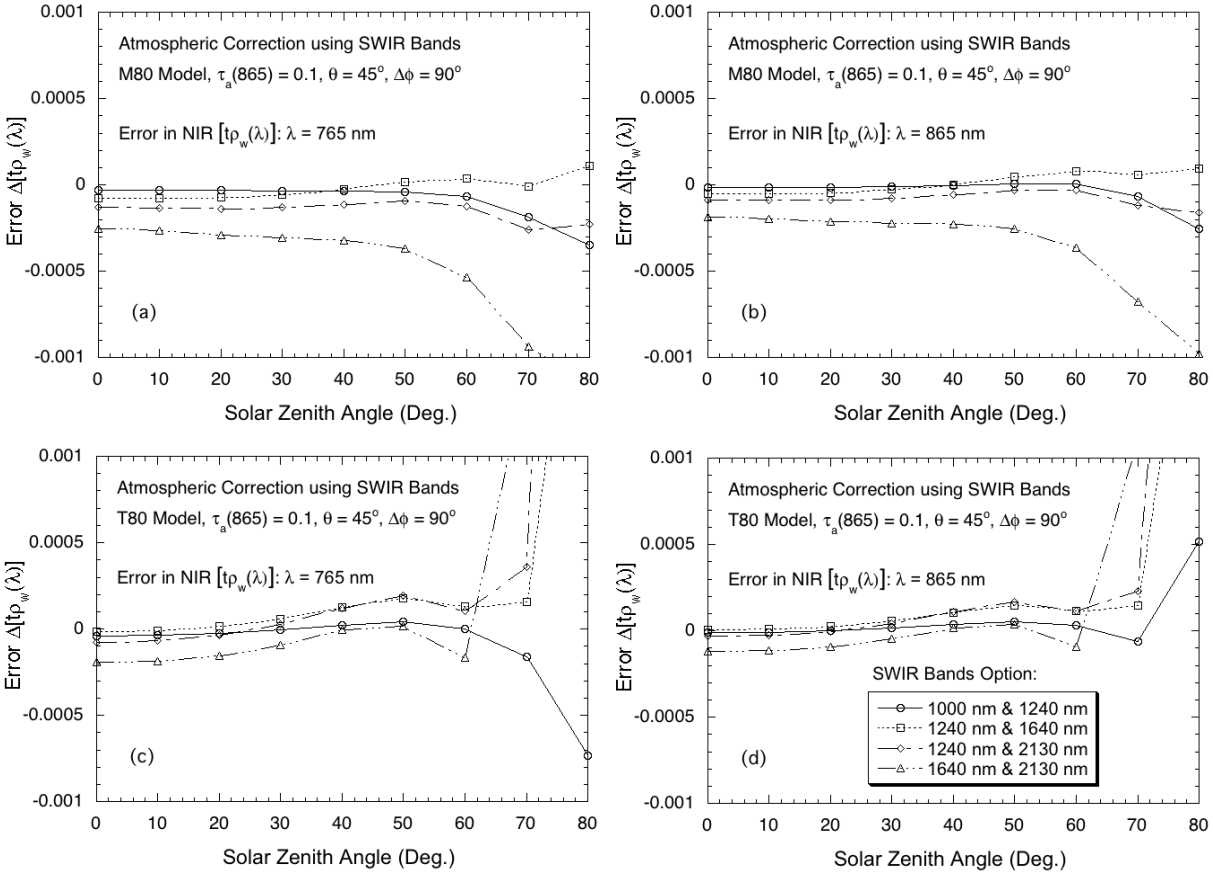

Figure 4. Error in the derived NIR water-leaving reflectance as a function of the solar-zenith angle for algorithm performed using the SWIR band combinations of 1000 and 1240 nm, 1240 and 1640 nm, 1240 and 2130 nm, and 1640 and 2130 nm and for derived at NIR wavelength with aerosol model of (a) and (b) 765 and 865 nm with the M80 model and (c) and (d) 765 and 865 nm with the T80 model (Wang, 2007)

To further assess the algorithm performance and quantify uncertainty using various combinations of the SWIR bands, simulations have been carried out for all applicable solar-sensor geometry with various aerosol optical properties. Simulations have been conducted for cases with the solar-zenith angles from 0°–80° at a step of 5°, the sensor-zenith angles from 0°–65° at a step of 5°, and the relative-azimuth angles from 0°–180° at a step of 10°, and for the M80 and T80 aerosol models with aerosol optical thicknesses 0.05, 0.1, and 0.2 at 865 nm. This is total of about 12000 cases (excluding sun glint cases) for each aerosol model (M80 or T80). Histograms and statistics for algorithm performance using the NIR bands and various combinations of the SWIR bands are generated and analyzed. Table 2 summarizes all the results that compare algorithm performance with various bands options for atmospheric correction. In Table 2, percentage of cases for a given error range in the derived water-leaving reflectance for

various options in atmospheric correction is provided for the M80 and T80 models. For example, for the UV (340 nm) water-leaving reflectance derived using the NIR bands (765 and 865 nm) method, there are 87.0%, 94.4%, and 98.4% of cases having uncertainty $\Delta[t\rho_w(\lambda)]$ within 5×10^{-4}, 1×10^{-3}, and 2×10^{-3} for the M80 model, respectively, while these percentages are 92.9%, 95.5%, and 97.6% for the T80 model. Comparing with results derived from the NIR bands, however, results from various SWIR band options for atmospheric correction show lower percentage values for the case with the M80 model, while for the T80 model the band option of 1000 and 1240 nm combination provides comparable results as those from the option of the two NIR bands. It is striking to note that algorithms with various band combination options performed as well for the short visible bands as for the UV band (340 nm). The water-leaving reflectance at the UV wavelengths (e.g., 340 nm) can be derived accurately due to significantly less aerosol reflectance contributions in the UV bands.

There are apparently two main factors affecting the performances of atmospheric correction with various band combination options (Table 2): (a) the wavelength distance needs to be extrapolated for the aerosol reflectance from the NIR (or SWIR) band and (b) the aerosol reflectance dispersion provided between two NIR or SWIR bands. Obviously, the aerosol reflectance can usually be more accurately extrapolated for the shorter wavelength distance than for the longer one. Thus, the NIR method generally produces slightly better results than those from the SWIR methods. On the other hand, larger dispersion of the aerosol reflectance between two NIR (or SWIR) bands with various aerosol models for atmospheric correction has a better sensitivity in deriving aerosol optical properties, leading to a better result in the derived water-leaving reflectances. For example, the SWIR method using bands 1240 and 2130 nm performed much better than that using bands 1640 and 2130 nm because the range of $\varepsilon(1240, 2130)$ for various aerosol models is significantly larger than that of $\varepsilon(1640, 2130)$, e.g., 0.98–4.76 vs. 1.04–2.46 in Fig. 1.

In summary, except for the method using the SWIR bands of 1640 and 2130 nm, atmospheric correction algorithm using the three SWIR band combinations (1000 and 1240 nm, 1240 and 1640 nm, and 1240 and 2130 nm) can produce comparable results as from the NIR band method for cases of non- and weakly absorbing aerosols, in particular, the SWIR-based atmospheric correction using the band set of 1240 and 2130 nm (MODIS case) can produce accurate water-leaving radiance spectra data.

TABLE 2. Algorithm performance comparisons using the NIR and various combinations of the SWIR bands (*Wang*, 2007).

λ (nm)	Two Bands for Atmospheric Correction (nm)	**% Cases for Range of $\|\Delta[t\,\rho_w(\lambda)]\|(\times 10^{-3})$**					
		M80 Model			T80 Model		
		≤ 0.5	≤ 1.0	≤ 2.0	≤ 0.5	≤ 1.0	≤ 2.0
340	765 & 865	87.0	94.4	98.4	92.9	95.5	97.6
	1000 & 1240	64.6	82.8	92.7	93.3	95.6	97.6
	1240 & 1640	70.9	84.6	93.8	86.7	92.1	94.7
	1240 & 2130	48.1	71.3	87.7	76.0	84.3	89.8
	1640 & 2130	23.5	45.5	72.7	75.8	81.4	86.6
412	765 & 865	89.7	95.4	98.4	91.9	94.6	96.6
	1000 & 1240	61.6	79.0	91.3	91.9	94.3	96.2
	1240 & 1640	68.1	81.6	91.7	83.3	88.8	92.1
	1240 & 2130	44.0	66.1	84.2	73.9	80.6	85.8
	1640 & 2130	18.8	38.1	63.0	69.0	77.9	82.7
443	765 & 865	92.9	96.9	98.6	92.4	94.6	96.6
	1000 & 1240	63.0	79.9	91.5	91.3	93.8	95.9
	1240 & 1640	69.9	82.3	91.6	82.8	87.8	91.3
	1240 & 2130	45.1	67.3	84.2	74.7	80.6	85.2
	1640 & 2130	19.0	38.2	62.8	66.7	77.6	82.3
490	765 & 865	93.6	97.1	98.7	92.5	94.6	96.6
	1000 & 1240	69.2	83.0	92.8	90.9	93.3	95.4
	1240 & 1640	74.4	85.0	92.5	82.2	86.6	90.4
	1240 & 2130	50.2	71.1	86.0	75.1	80.1	84.6
	1640 & 2130	22.3	40.3	64.9	66.3	77.3	81.7
510	765 & 865	96.0	97.9	98.8	92.7	94.7	96.7
	1000 & 1240	69.9	83.8	93.2	90.8	93.2	95.4
	1240 & 1640	75.0	85.6	92.6	82.3	86.4	90.2
	1240 & 2130	51.7	71.9	86.2	75.4	80.2	84.5
	1640 & 2130	23.1	40.9	65.4	67.0	77.4	81.7
555	765 & 865	97.7	98.4	98.8	93.6	95.3	96.8
	1000 & 1240	76.3	87.7	95.0	90.4	93.1	95.2
	1240 & 1640	79.5	87.8	93.7	83.1	86.2	89.9
	1240 & 2130	59.9	76.3	88.4	76.8	81.1	84.8
	1640 & 2130	27.0	44.2	68.9	66.5	78.0	82.0

2.3.3. NIR-SWIR combined atmospheric correction algorithm

Wang and Shi (2007) described and demonstrated a NIR-SWIR combined method for the atmospheric correction for the MODIS ocean color data processing. In this new method, pixels in ocean regions with significant ocean NIR contributions (i.e., turbid waters) can first be discriminated using MODIS measurements. The turbid waters are detected using the turbid water index that is computed from the MODIS-measured radiances at the NIR and SWIR bands. The turbid water index, T_{ind}, can be derived as (*Shi and Wang*, 2007b):

$$T_{ind} = 1 + t(748)\,\rho_w(748) / \rho_A(748), \quad (8)$$

where $t(748)\rho_w(748)$ and $\rho_A(748)$ are the TOA water-leaving reflectance and aerosol reflectance (including Rayleigh-aerosol interactions) at the wavelength of 748 nm, respectively.

The turbid water detection is operated prior to the atmospheric correction procedure and is very efficient. For the identified turbid water pixels, the SWIR atmospheric correction algorithm can then be applied. For the most other pixels (non-turbid ocean waters), the standard (NIR) atmospheric correction algorithm can be employed. Thus, while the ocean color products in the coastal regions can be improved using the SWIR method, the MODIS high quality ocean color data in open oceans can be continuously produced. In the data processing system, the NIR-SWIR algorithm is switched on in the input parameter file, and the threshold for detecting the turbid water is set to 1.05. The flow chart of the data processing is shown in Figure 5.

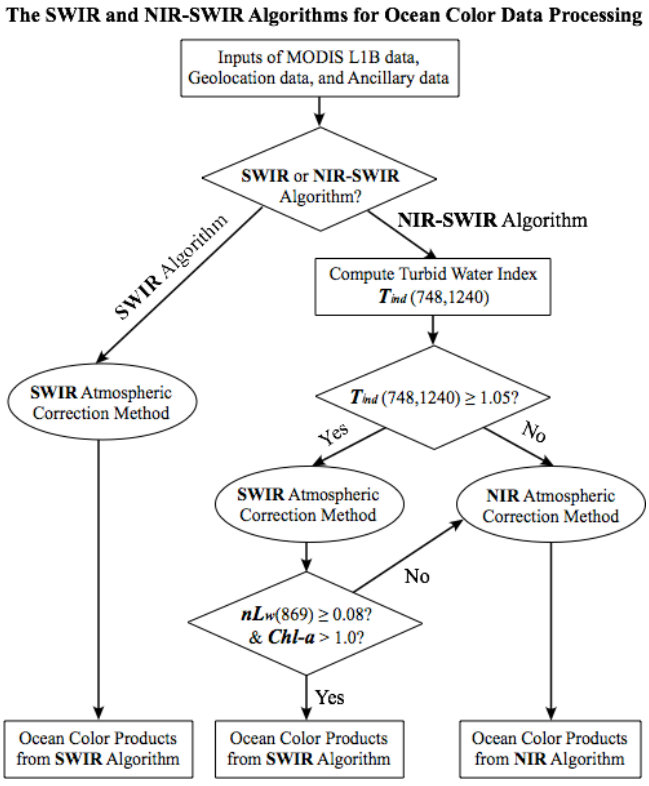

Figure 5. MODIS NIR-SWIR-based data processing flow chart (*Wang and Shi*, 2007).

2.3.4. K_d(490) algorithm description

The proposed K_d(490) algorithm is a combination of a turbid water algorithm (*Wang, et al.*, 2009a) and a clear open ocean algorithm (*Mueller*, 2000). *Wang et al.* (2009a) described a new K_d(490) algorithm for turbid water:

$$K_d(490) = \frac{2.697\times10^{-4}}{R(488)} + 1.045\frac{R(667)}{R(488)} + 4.18\left[7\times10^{-4} + 2.7135R(667)\right] \times\left\{1-0.52\exp\left[-\frac{2.533\times10^{-3}}{R(488)} - 9.817\frac{R(667)}{R(488)}\right]\right\}, \quad (9)$$

where $R(\lambda)$ is the irradiance reflectance beneath the sea surface. $R(\lambda)$ can be calculated from the MODIS-derived normalized water-leaving radiance, $nL_w(\lambda)$:

$$R(\lambda) = \frac{4\,nL_w(\lambda)}{0.52\,F_0(\lambda) + 1.7\,nL_w(\lambda)}, \quad (10)$$

where $F_0(\lambda)$ is the extraterrestrial solar irradiance at a given wavelength λ.

For clear open ocean waters, the *Mueller* (2000) algorithm is used:

$$K_d(490) = K_w(490) + A\cdot\left(\frac{nL_w(490)}{nL_w(555)}\right)^B \quad (11)$$

where $K_w(490) = 0$, $A = 0.1853$, and $B = -1.349$.

The combined new K_d(490) model are expressed as:

$$K_d^{Comb}(490) = (1-W)K_d^{Clear}(490) + W\,K_d^{Turbid}(490)\ , \quad (12)$$

where the weighting function is computed as:

$$W = -1.175 + 4.512\frac{R_{rs}(670)}{R_{rs}(490)}\ \text{, for } 0.2604 \le \frac{R_{rs}(670)}{R_{rs}(490)} \le 0.4821. \quad (13)$$

It is noted that $W = 0$ for $W \le 0$ and $W = 1$ for $W \ge 1$. In Eq. (9), K_d^{Clear}(490) is the model for open oceans, i.e., from *Mueller* (2000) (Eq. (11)), and K_d^{Turbid}(490) is the model for turbid coastal waters (Eq. (9)). Thus, for values of $K_d(490) \le 0.3$ m^{-1}, K_d^{Comb}(490) in Eq. (12) produces diffuse attenuation coefficient using the K_d^{Clear}(490) model, while for values of $K_d(490) \ge 0.6$ m^{-1} the K_d^{Turbid}(490) model is used in Eq. (9). For values of $K_d(490)$ between 0.3–0.6 m^{-1}, a weight according to Eq. (13) is used to combine values produced from models of K_d^{Clear}(490) and K_d^{Turbid}(490) (*Wang, et al.*, 2009a).

2.4. Algorithm Output

The MODIS NIR-SWIR algorithm generates a Level-2 data file in HDF-4 format, which has the same data structure as the existing operational MODIS ocean color data processing output. Specifically, the output Level-2 file contains the following data products: $nL_w(\lambda)$ for MODIS bands at 412, 443, 488, 531, 551, and 667 nm, chlorophyll-a concentration, remote sensing reflectance $R_{rs}(667)$, and $K_d(490)$.

2.5. Algorithm Validation

2.5.1. NIR-SWIR-based atmosphere correction algorithm validation

Figure 6 show a sample image along U.S. east coast region generated by *Wang and Shi* (2007) using three algorithms: NIR, SWIR, and NIR-SWIR atmospheric correction algorithms. Results in the top panel of Figs. 6(a)–6(d) are MODIS-Aqua-derived chlorophyll-a (Chl-a) concentration and $nL_w(\lambda)$ at wavelengths of 443 nm ($nL_w(443)$), 531 nm ($nL_w(531)$), and 667 nm ($nL_w(667)$), respectively, which were obtained using the standard-NIR data processing approach. Figures 6(e)–6(h) (the middle panel) are results corresponding to the same parameters derived using the SWIR atmospheric correction method, while images in Figs. 6(i)–6(l) (the bottom panel) are the corresponding results from using the NIR-SWIR combined data processing approach. Judging the results by examining overall image quality (e.g., data smoothness, number of missing data, etc.), Fig. 6 shows that, while the standard-NIR method produces good quality ocean color products further offshore, the standard data processing outputs results with noticeable noise and significant missing data in the coastal regions, e.g., regions in and/or around the Chesapeake Bay, Outer Banks, and Delaware Bay. Alternatively, results in Figs. 6(e)–6(h) show that the SWIR algorithm can significantly improve the ocean color products in the coastal near-shore regions, but further offshore there is substantial noise and data dropout in the derived products, e.g., results from regions around the northern Delaware Bay. Thus, the advantages of using the NIR-SWIR combined method for the MODIS ocean color data processing are readily demonstrated in Figs. 6(i)–6(l). The new method has not only produced improved ocean color products in near-shore coastal regions, it also has preserved the high quality data products in further offshore.

Using the NASA maintained ocean optical and biological in situ data that were collected during 2002–2005, *Wang et al.* (2009b) evaluated the performance of atmospheric correction algorithms for the ocean color products from MODIS on the Aqua satellite. Specifically, algorithms using the SWIR bands and NIR-SWIR combined method are evaluated, compared to the match-up results from the standard NIR-based algorithm. Fig. 7 shows the comparison between the MODIS-derived and in situ measured ocean color products for various cases. The ocean color products included in these results are the normalized water-leaving radiance $nL_w(\lambda)$ at wavelengths of 412, 443, 488, 531, 551, and 667 nm, Chl-a, and the diffuse attenuation coefficient at the wavelength 490 nm ($K_d(490)$). Figs. 7(a), 7(c), and 7(e) show $nL_w(\lambda)$ comparisons, while Figs. 7(b), 7(d), and 7(f) are evaluations for products Chl-a and $K_d(490)$. Figs. 7(a), 7(c), and 7(e) are MODIS-derived $nL_w(\lambda)$ results compared with the in situ

measurements, corresponding to cases for which MODIS-Aqua data are processed using the standard–NIR, SWIR, and NIR–SWIR combined method, respectively. Figs. 7(b), 7(d), and 7(f) are results of the Chl-a and K_d(490) match-ups corresponding to MODIS data processed with the three different algorithms.

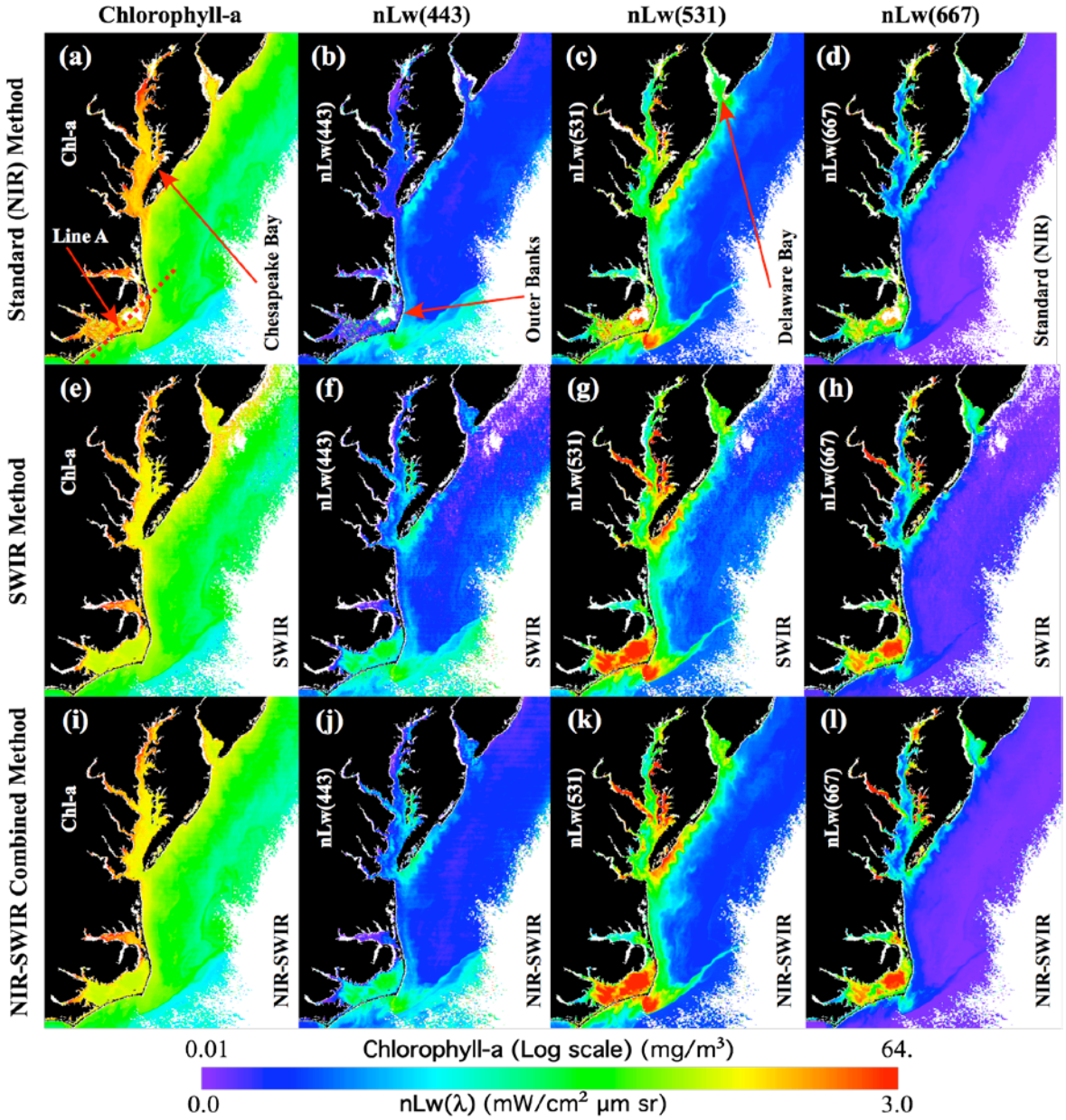

Figure 6. The MODIS-Aqua measurements acquired along the U.S. east coast region on April 5, 2004 for the images of Chl-a, nL_w(443), nL_w(531), and nL_w(667), respectively. Panels (a)-(d) are results from the standard (NIR) method; panels (e)-(h) are results from the SWIR method; and panels (i)-(l) are results from the NIR-SWIR combined method (*Wang and Shi*, 2007).

For the $nL_w(\lambda)$ results, the slopes of the overall match-ups using the SWIR and NIR–SWIR methods (Figs. 7(c) and 7(e)) have been improved compared with those using the standard-NIR method (Fig. 7(a)). However, the SWIR method produced increased product noise (*Wang and Shi*, 2012), which can be seen in Fig. 7 and is also indicated from the reduced correlation coefficient for the match-ups. The slopes in the overall $nL_w(\lambda)$ match-ups for the standard, SWIR, and NIR-SWIR methods are 0.841, 0.949, and 0.962 with their corresponding correlation coefficients of 0.910, 0.866, and 0.929, respectively. The data noise produced by the SWIR method is due mainly to the substantially lower sensor SNR values for the MODIS SWIR bands (*Wang and Shi*, 2012) and also because of SWIR algorithm performance errors (*Wang*, 2007). Similar results are also shown for the Chl-a and $K_d(490)$ match-up comparisons (Figs. 7(b), 7(d), and 7(f)); in particular, results from the SWIR method show lower correlation coefficient values.

The standard-NIR, SWIR, and NIR–SWIR algorithm performances are further evaluated with the MODIS-Aqua global ocean color product data. Fig. 8 provides color images for global composite distributions of MODIS-Aqua Chl-a and $nL_w(443)$ for the month of July 2005, which were derived using the standard-NIR, SWIR, and NIR-SWIR combined methods from MODIS-Aqua global measurements. Figs. 8(a), 8(c), and 8(d) are color images of Chl-a for MODIS-Aqua data that were processed using the standard-NIR, SWIR, and NIR-SWIR method, respectively, while Figs. 8(b), 8(d), and 8(f) are the corresponding $nL_w(443)$ images from the three different data processing methods. The product images for the standard-NIR method (Figs. 8(a) and 8(b)) were downloaded directly from the NASA ocean color website, while results of the SWIR and NIR-SWIR combined methods (Figs. 8(c)–8(f)) were generated from the MODIS-Aqua L1B data (July of 2005) using the SWIR and NIR-SWIR method, respectively. These images compare the global spatial variations of the ocean color products (Chl-a and $nL_w(443)$) that were derived from three different methods. It is noted that there is a solar-zenith angle cut off at 70° for all three data processing methods. Results in Fig. 8 show that, for the most of ocean regions, all three methods produced similar monthly Chl-a and $nL_w(443)$ data distributions. However, Fig. 8 shows some obvious differences in MODIS-derived Chl-a and $nL_w(443)$ from three methods. Both SWIR and NIR-SWIR methods show some improved data coverage, e.g., along the China east coastal region, while the SWIR method produced some obvious different results in some open ocean regions, e.g., in the southern ocean. Judging data quality by their coverage, spatial continuity, and image smoothness, it appears that the NIR-SWIR method produced the best Chl-a and $nL_w(443)$ results.

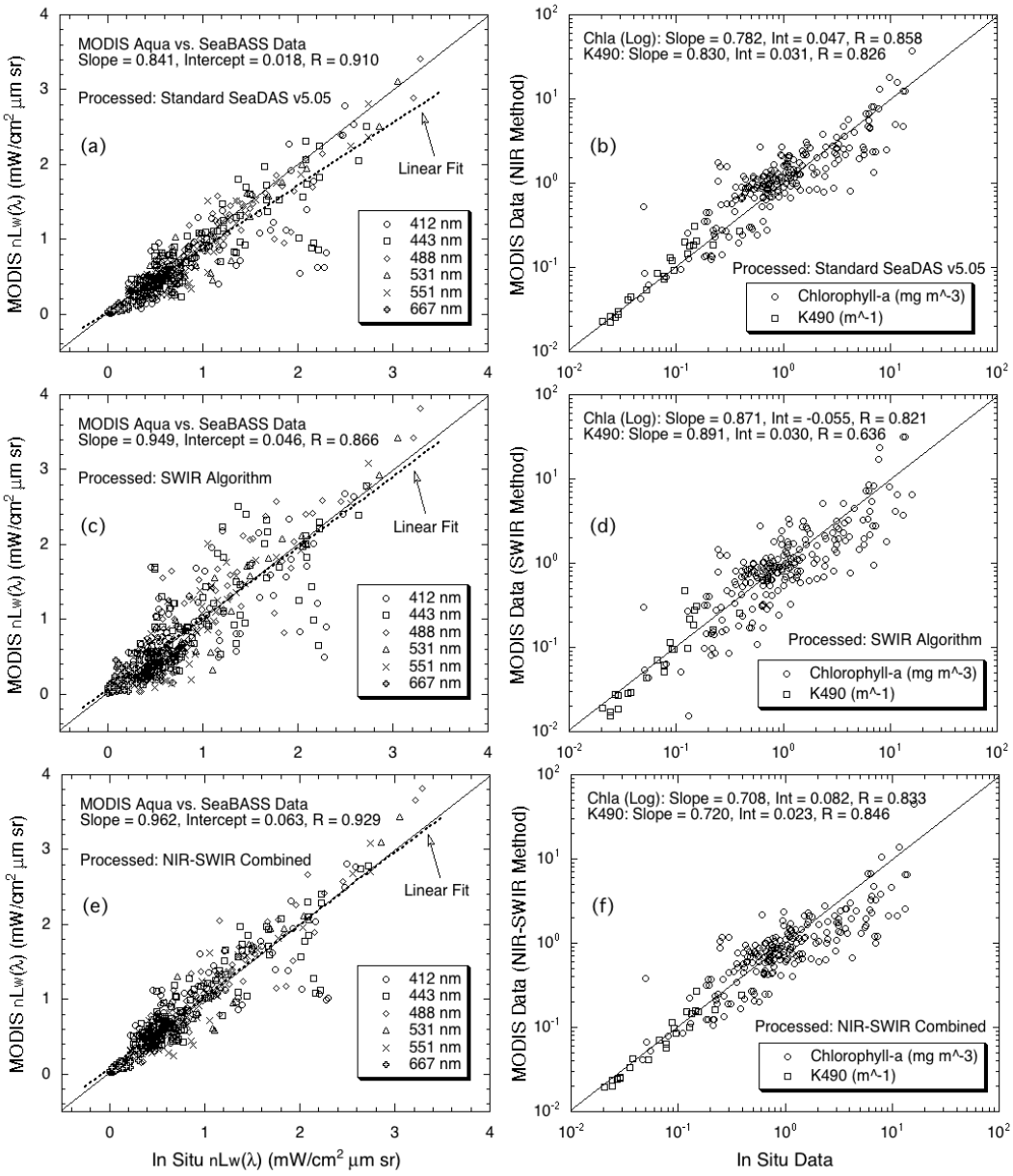

Figure 7. MODIS-derived nLw(λ), Chl-a and K490 compared with in situ measurements using (a) and (b) the standard algorithm, (c) and (d) the SWIR algorithm, and (e) and (f) the NIR–SWIR combined method (Wang et al., 2009b).

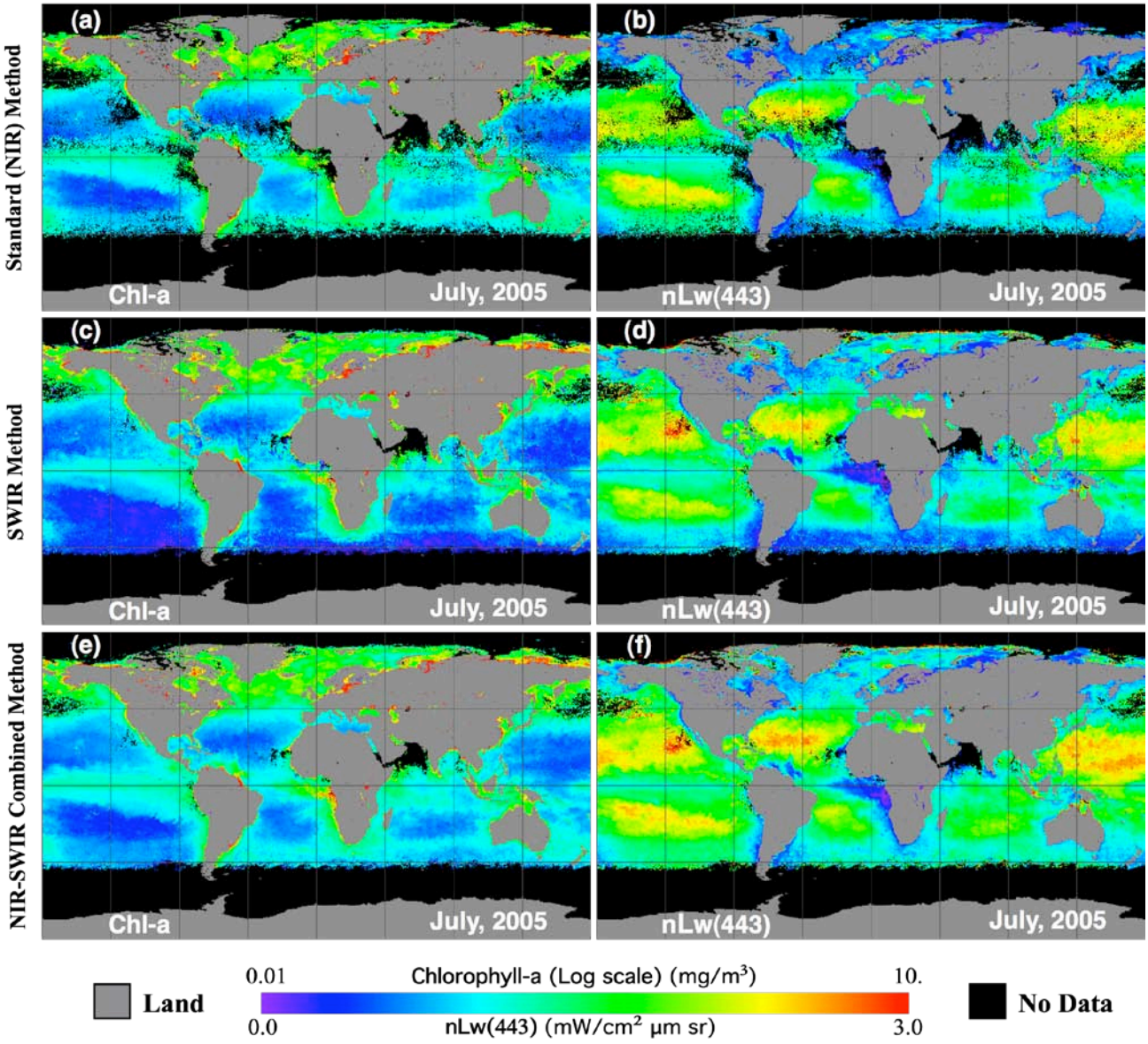

Figure 8. Color images for the global composite distribution of the MODIS-Aqua derived Chl-a and $nL_w(443)$ for the month of July 2005, which were retrieved using (a) and (b) the standard (NIR) algorithm, (c) and (d) the SWIR method, and (e) and (f) the NIR–SWIR combined method (Wang et al., 2009b).

2.5.2. K_d(490) algorithm validation

Wang et al. (2009a) compared the model-derived K_d(490) values using Eq. (12) and in-situ measured data. Note that the model K_d(490) data were derived using Eq. (12) with the in-situ-measured reflectance data from SeaBASS data set. In Fig. 9, two sets of the in situ K_d(490) data (all from SeaBASS), one from the Chesapeake Bay region and another from global non-Chesapeake Bay data, are used. The Chesapeake Bay K_d(490) data have generally high values ranging from 0.4–5 m^{-1}, while the non-Chesapeake Bay in situ data have K_d(490) values ranging from 0.02–3.7 m^{-1} covering deep clear oceans (e.g., oligotrophic waters) to some coastal turbid waters. Results in Fig. 9 verified the new algorithm performance for the Chesapeake Bay region.

The proposed new K_d(490) algorithm has been further evaluated for producing MODIS-Aqua global ocean K_d(490) product data. Figure 10 provides color images for global composite distributions of the MODIS-Aqua K_d(490) for the months of January and July 2005 derived using the NIR-SWIR-combined atmospheric correction algorithm for the MODIS-Aqua data processing. Figures 10(a) and 10(c) are color images of K_d(490) derived from the *Mueller* (2000) model for month of January and July 2005, respectively, and Figures 10(b) and 10(d) are global K_d(490) images obtained using the new proposed algorithm K_d^{Comb}(490) with the *Mueller* (2000) model for the corresponding K_d^{Clear}(490) computations. Results in Figure 10 show that for the open oceans both the new model and the *Mueller* (2000) model produced the same K_d(490) data (as designed), whereas for coastal regions the new algorithm produced significantly higher K_d(490) values than the *Mueller* (2000) model. Therefore, using the proposed new approach to derive a K_d(490) product, K_d(490) product data in turbid coastal waters can be improved while excellent K_d(490) results are still generated for open ocean regions.

2.5.3. Other validation efforts and various applications

NOAA/STAR has been continuously processing the MODIS-Aqua ocean color data using the NIR-SWIR algorithm since 2009, and the data output, including normalized water-leaving radiance spectra $nL_w(\lambda)$, chlorophyll-a concentration, and water diffuse attenuation coefficient K_d(490), have been evaluated by the CoastWatch QA/QC team routinely. In addition, ocean-color products derived from the SWIR-based atmospheric correction have been shown to have various important applications, such as study of storm-driven phytoplankton blooms (*Liu et al.*, 2009; *Shi and Wang*, 2007a) and storm-induced sediment re-suspension (*Shi and Wang*, 2008), storm-water runoff plume detection (*Nezlin et al.*, 2008), ocean optical and biological property variations in the Korean dump site of the Yellow Sea (*Son et al.*, 2011), macro-algae blooms (*Shi and Wang*, 2009b), flood-driven river plume dynamics (*Shi and Wang*, 2009a), environmental responses to a land reclamation project in South Korea (*Son and Wang*, 2009), satellite observations of the seasonal sediment plume in central East China Sea (*Shi and Wang*, 2010b), global ocean turbidity characterization (*Shi and Wang*, 2010a), ocean sand ridge signatures in the Bohai Sea (*Shi et al.*, 2011b), spring-neap tidal effects on satellite ocean color observations (*Shi et al.*, 2011a), and inland fresh water monitoring and management (*Wang and Shi*, 2008; *Wang et al.*, 2011). Using the SWIR-based atmospheric correction approach, the sea ice property in the Bohai Sea can be derived and used for study of regional sea ice seasonal and interannual

variability (*Shi and Wang*, 2012a; 2012b). In addition, with the SWIR-based atmospheric correction method, NIR ocean contributions can also be derived accurately and used for retrieval of ocean properties such as sediment concentration.

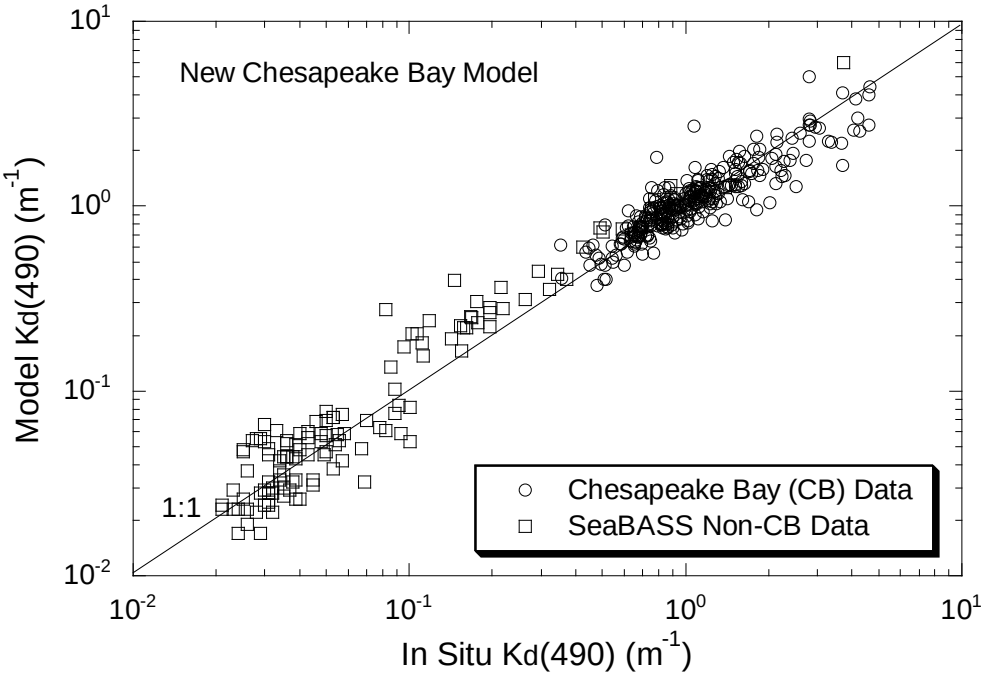

Figure 9. $K_d(490)$ comparison results of the new model-derived values and in situ measurements from the Chesapeake Bay and global SeaBASS (excluding Chesapeake Bay) data sets (Wang et al. (2009).

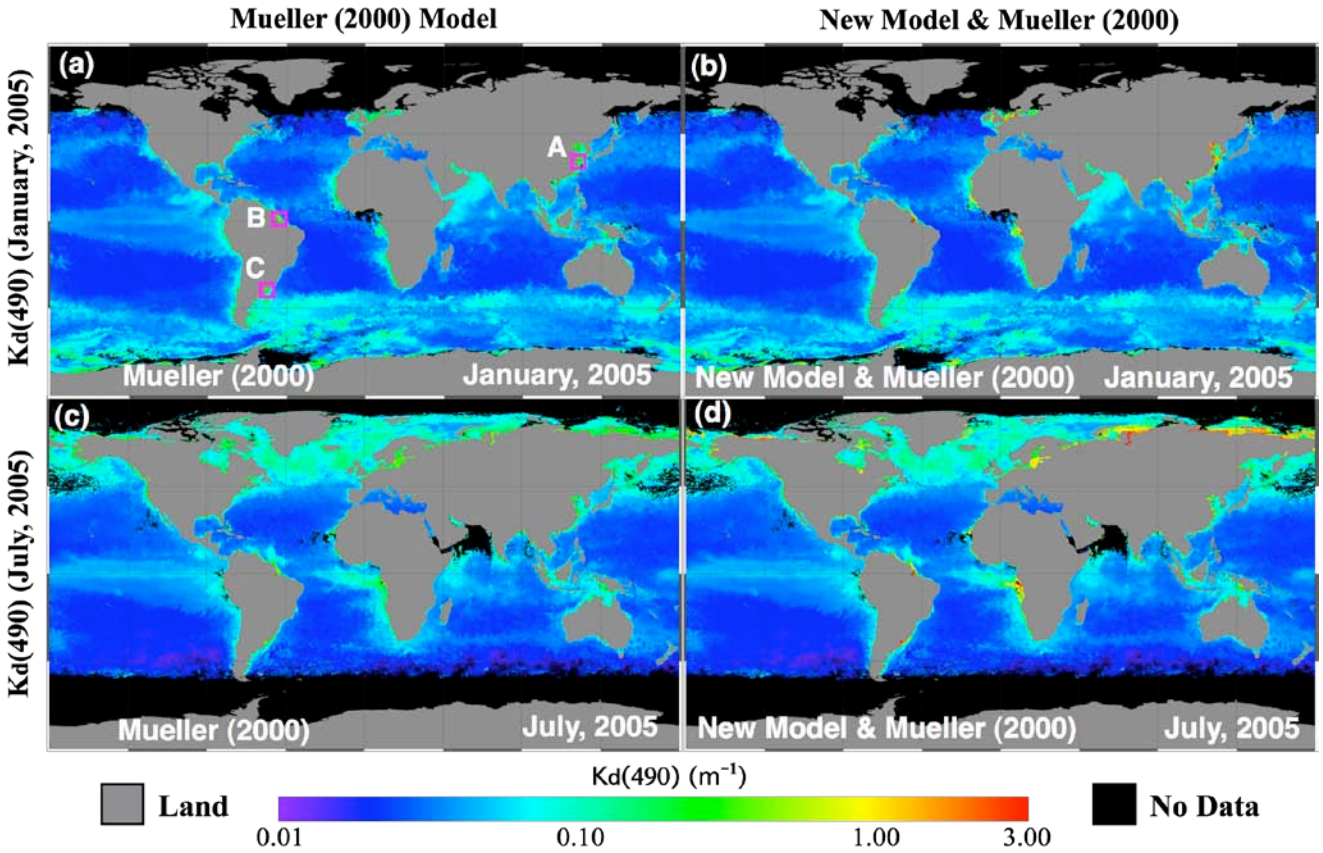

Figure 10. MODIS-Aqua-derived global $K_d(490)$ composite images for the months of (a and b) January and (c and d) July 2005. (a) and (c) are derived using the Mueller [2000] model, while (b) and (d) are obtained using the new proposed algorithm with the Mueller [2000] model for the corresponding K_d Clear $K_d(490)$ computations in equation (12) (Wang et al., 2009).

3. ASSUMPTIONS AND LIMITATIONS

3.1. Assumptions

1. In the proposed NIR-SWIR combined method for the atmospheric correction, the black ocean is assumed in the NIR bands in the NIR-based algorithm for clear water pixels (however, with some modifications for NIR ocean contributions for some productive waters), and in SWIR bands in the SWIR-based algorithm for turbid water pixels.
2. Non- or weakly absorbing aerosols are assumed in the atmosphere correction algorithm and ocean color data processing.

3.2. Limitations

3.2.1. Noise issue for the MODIS SWIR bands

The match-up analysis demonstrates that using the MODIS SWIR bands for ocean color data processing has reduced the bias errors in $nL_w(\lambda)$. However, the noise errors are increased (*Wang, et al.*, 2009b; *Werdell, et al.*, 2010), possibly leading to some negative $nL_w(\lambda)$ cases for which true $nL_w(\lambda)$ values are very low. Comparing to the results from the standard-NIR method, however, the SWIR method improves the MODIS-derived $nL_w(\lambda)$ products in the coastal regions, where true $nL_w(\lambda)$ values at the blue (412 and 443 nm) are often quite low. In these cases, we found that using the SWIR method the MODIS $nL_w(\lambda)$ values at the blue are elevated (*Wang and Shi*, 2007; *Wang et al.*, 2007) and cases with the negative $nL_w(\lambda)$ are in fact reduced significantly. Therefore, in the coastal ocean regions, the SWIR method is usually superior to the NIR method, particularly over the turbid waters. It is important to note that, for both the SWIR and NIR-SWIR algorithms, bias errors in $nL_w(\lambda)$ from the match-up analysis are reduced, indicating improved algorithm performance also related to the improved aerosol lookup tables with the vicarious calibration.

The data product noise errors from the SWIR method are mainly from two sources: (1) considerably lower SNR values for the MODIS SWIR bands that are used for the data processing (atmospheric correction) and (2) a little more uncertainty introduced by using the SWIR bands (1240 and 2130 nm) for atmospheric correction (*Wang and Shi*, 2012). A recent study (*Wang*, 2007) shows that atmospheric correction using the SWIR bands (1240 and 2130 nm) for deriving $nL_w(\lambda)$ often produces a little larger uncertainty than results from the NIR bands (748 and 869 nm). This is particularly true for cases of the maritime aerosols, which are often dominated in the open oceans. In addition, with the current MODIS SNR characteristics for the SWIR bands, there is significant noise in the derived $nL_w(\lambda)$ using the SWIR algorithm (*Wang*, 2007). Therefore, it is proposed that MODIS-Aqua ocean color products be processed using the NIR-SWIR combined method for which the non-turbid and turbid ocean waters are processed using the standard-NIR and SWIR method, respectively.

For the turbid coastal waters, the use of the MODIS SWIR algorithm versus the standard-NIR algorithm with the NIR ocean contribution correction is somewhat a tradeoff between using a noised measurement with little or no bias versus a high quality radiance measurement with a correction algorithm that is in error. However, it is generally desired to use the satellite-measured

data instead of modeling for the NIR ocean contribution correction because of model limitations, particularly over very turbid waters. Thus, the SWIR algorithm is preferred for deriving water properties in the coastal and inland turbid waters.

3.2.2. Issue with strongly absorbing aerosols

The NIR-SWIR-based ocean color data processing also assumes that aerosols are non- and weakly absorbing. For strongly absorbing aerosols, e.g., dust, smoke, results from the current atmospheric correction algorithm are poor. An essential problem for the absorbing aerosol correction in deriving accurate ocean color products is principally due to aerosol particle absorbing characteristics at the visible bands. Some studies for the effects of the absorbing aerosols on the atmospheric correction for ocean color products have been conducted (*Chomko and Gordon*, 1998; *Chomko et al.*, 2003; *Gordon*, 1997; *Gordon et al.*, 1997). It is now well known that for the strongly absorbing aerosols the sensor-measured TOA radiances depend strongly on aerosol layer vertical profile. Thus, for accurate atmospheric correction for the absorbing aerosols, one will require information of the aerosol layer vertical location. It is generally difficult to obtain aerosol vertical distribution profile from passive radiance measurements, in particular, for a thin aerosol layer. In addition, realistic aerosol models (e.g., dust model) that are representative regionally are required. These absorbing aerosol models are needed for generating the aerosol lookup tables that will be used for the atmospheric correction. The current NIR-SWIR-based atmospheric correction has not yet included absorbing aerosol models for dealing with absorbing aerosol cases. In addition, aerosol vertical distributions for absorbing aerosols are not available. However, absorbing aerosol cases can be identified using MODIS measurements at short visible, NIR, and SWIR bands (*Shi and Wang*, 2007b), and can be used for data quality assurance purpose.

4. LIST OF REFERENCES

Ahmad, Z., Franz, B. A., McClain, C. R., Kwiatkowska, E. J., Werdell, J., Shettle, E. P., and Holben, B. N. (2010), New aerosol models for the retrieval of aerosol optical thickness and normalized water-leaving radiances from the SeaWiFS and MODIS sensors over coastal regions and open oceans, *Appl. Opt.*, *49*, 5545-5560.

Antoine, D., and Morel, A. (1999), A multiple scattering algorithm for atmospheric correction of remotely sensed ocean colour (MERIS instrument): principle and implementation for atmospheres carrying various aerosols including absorbing ones, *Int. J. Remote Sens.*, *20*, 1875-1916.

Bailey, S. W., Franz, B. A., and Werdell, P. J. (2010), Estimation of near-infrared water-leaving reflectance for satellite ocean color data processing, *Optics Express*, *18*, 7521-7527.

Behrenfeld, M. J., O'Malley, R. T., Siegel, D. A., McClain, C. R., Sarmiento, J. L., Feldman, G. C., Milligan, A. J., Falkowski, P. G., Letelier, R. M., and Boss, E. S. (2006), Climate-driven trends in contemporary ocean productivity, *Nature*, *444*, 752-755.

Behrenfeld, M. J., Randerson, J. T., McClain, C. R., Feldman, G. C., Los, S. O., Tucker, C. J., Falkowski, P. G., Field, C. B., Frouin, R., Esaias, W. E., Kolber, D. D., and Pollack, N. H. (2001), Biospheric primary production during an ENSO transition, *Science*, *291*, 2594-2597.

Chavez, F. P., Strutton, P. G., Friederich, G. E., Feely, R. A., Feldman, G. C., Foley, D. G., and McPhaden, M. J. (1999), Biological and Chemical Response of the Equatorial Pacific Ocean to the 1997-98 El Niño, *Science*, *286*, 2126-2131.

Chomko, R., and Gordon, H. R. (1998), Atmospheric correction of ocean color imagery: use of the Junge power-law aerosol size distribution with variable refractive index to handle aerosol absorption, *Appl. Opt.*, *37*, 5560-5572.

Chomko, R. M., Gordon, H. R., Maritorena, S., and Siegel, D. A. (2003), Simultaneous retrieval of oceanic and atmospheric parameters for ocean color imagery by spectral optimization: a validation, *Remote Sens. Environ.*, *84*, 208-220.

Cox, C., and Munk, W. (1954), Measurements of the roughness of the sea surface from photographs of the sun's glitter, *Jour. Opt. Soc. of Am.*, *44*, 838-850.

Deschamps, P. Y., Herman, M., and Tanre, D. (1983), Modeling of the atmospheric effects and its application to the remote sensing of ocean color, *Appl. Opt.*, *22*, 3751-3758.

Esaias, W. E., Abbott, M. R., Barton, I., Brown, O. B., Campbell, J. W., Carder, K. L., Clark, D. K., Evans, R. L., Hodge, F. E., Gordon, H. R., Balch, W. P., Letelier, R., and Minnet, P. J. (1998), An overview of MODIS capabilities for ocean science observations, *IEEE Trans. Geosci. Remote Sens.*, *36*, 1250-1265.

Frouin, R., Schwindling, M., and Deschamps, P. Y. (1996), Spectral reflectance of sea foam in the visible and near infrared: In situ measurements and remote sensing implications, *J. Geophys. Res.*, *101*, 14,361-314,371.

Fukushima, H., Higurashi, A., Mitomi, Y., Nakajima, T., Noguchi, T., Tanaka, T., and Toratani, M. (1998), Correction of atmospheric effects on ADEOS/OCTS ocean color data: Algorithm description and evaluation of its performance, *J. Oceanogr.*, *54*, 417-430.

Gordon, H. R. (1997), Atmospheric correction of ocean color imagery in the Earth Observing System era, *J. Geophys. Res.*, *102*, 17081–17106.

Gordon, H. R., Brown, J. W., and Evans, R. H. (1988), Exact Rayleigh scattering calculations for use with the Nimbus-7 Coastal Zone Color Scanner, *Appl. Opt.*, *27*, 862-871.

Gordon, H. R., Clark, D. K., Mueller, J. L., and Hovis, W. A. (1980), Phytoplankton Pigments from the Nimbus-7 Coastal Zone Color Scanner: Comparisons with Surface Measurements, *Science*, *210*, 63-66.

Gordon, H. R., Du, T., and Zhang, T. (1997), Remote sensing of ocean color and aerosol properties: resolving the issue of aerosol absorption, *Appl. Opt.*, *36*, 8670-8684.

Gordon, H. R., and Wang, M. (1992), Surface roughness considerations for atmospheric correction of ocean color sensors. 1: The Rayleigh scattering component, *Appl. Opt.*, *31*, 4247-4260.

Gordon, H. R., and Wang, M. (1994a), Retrieval of water-leaving radiance and aerosol optical thickness over the oceans with SeaWiFS: A preliminary algorithm, *Appl. Opt.*, *33*, 443-452.

Gordon, H. R., and Wang, M. (1994b), Influence of oceanic whitecaps on atmospheric correction of ocean-color sensor, *Appl. Opt.*, *33*, 7754-7763.

Hale, G. M., and Querry, M. R. (1973), Optical constants of water in the 200nm to 200µm wavelength region, *Appl. Opt.*, *12*, 555-563.

Hooker, S. B., Esaias, W. E., Feldman, G. C., Gregg, W. W., and McClain, C. R. (1992), An Overview of SeaWiFS and Ocean Color, Vol. 1 of SeaWiFS Technical Report Series,NASA Tech. Memo. 104566, S.B. Hooker and E.R. Firestone, Eds., p, NASA Goddard Space Flight Center, Greenbelt, Maryland.

Hovis, W. A., Clark, D. K., Anderson, F., Austin, R. W., Wilson, W. H., Baker, E. T., Ball, D., Gordon, H. R., Mueller, J. L., Sayed, S. T. E., Strum, B., Wrigley, R. C., and Yentsch, C. S. (1980), Nimbus 7 Coastal Zone Color Scanner: system description and initial imagery, *Science*, *210*, 60-63.

IOCCG, Atmospheric Correction for Remotely-Sensed Ocean-Colour Products, Wang, M. (Ed.), (2010), *Reports of International Ocean-Color Coordinating Group,* No. 10, IOCCG, Dartmouth, Canada.

Kou, L., Labrie, D., and Chylek, P. (1993), Refractive indices of water and ice in the 0.65-2.5µm spectral range, *Appl. Opt.*, *32*, 3531-3540.

Lavender, S. J., Pinkerton, M. H., Moore, G. F., Aiken, J., and Blondeau-Patissier, D. (2005), Modification to the atmospheric correction of SeaWiFS ocean color images over turbid waters, *Continental Shelf Research*, *25*, 539-555.

Lee, Z. P., Carder, K. L., and Arnone, R. A. (2002), Deriving inherent optical properties from water color: a multiple quasi-analytical algorithm for optically deep waters, *Appl. Opt.*, *41*, 5755-5772.

Lewis, M., Carr, M., Feldman, G., Esaias, W. E., and McClain, C. R. (1990), Influence of penetrating solar radiation on the heat budget of the equatorial Pacific ocean, *Nature*, *347*, 543-545.

Liu, X., Wang, M., and Shi, W. (2009), A study of a Hurricane Katrina-induced phytoplankton bloom using satellite observations and model simulations, *J. Geophys. Res.*, *114*, C03023, doi:10.1029/2008JC004934.

McClain, C. R. (2009), A decade of satellite ocean color observations, *Annual Review of Marine Science*, *1*, 19-42.

McClain, C. R., Feldman, G. C., and Hooker, S. B. (2004), An overview of the SeaWiFS project and strategies for producing a climate research quality global ocean bio-optical time series, *Deep-Sea Research Part II-Topical Studies in Oceanography*, *51*, 5-42.

Moore, K. D., Voss, K. J., and Gordon, H. R. (2000), Spectral reflectance of whitecaps: Their contribution to water-leaving radiance, *J. of Geophys. Res.*, *105*, 6493-6499.

Morel, A., and Antoine, D. (1994), Heating rate within the upper ocean in relation to its bio-optical state, *J. Phys. Oceanogr.*, *24*, 1652-1665.

Morel, A., Huot, Y., Gentili, B., Werdell, P. J., Hooker, S. B., and Franz, B. A. (2007), Examining the consistency of products derived from various ocean color sensors in open ocean (Case 1) waters in the perspective of a multi-sensor approach, *Remote Sens. Environ.*, *111*, 69-88.

Mueller, J. L. (2000), SeaWiFS algorithm for the diffuse attenuation coefficient, K(490), using water-leaving radiances at 490 and 555 nm, SeaWiFS Postlaunch Technical Report Series,Vol. 11, NASA Tech. Memo. 2000-206892, S. B. Hooker and E. R. Firestone, Eds., p24-27, NASA Goddard Space Flight Center, Greenbelt, Maryland.

Nezlin, N. P., DiGiacomo, P. M., Diehl, D. W., Jones, B. H., Johnson, S. C., Mengel, M. J., Reifel, K. M., Warrick, J. A., and Wang, M. (2008), Stormwater plume detection by MODIS imagery in the southern California coastal ocean, *Estuarine, Coastal and Shelf Science*, *80*, 141-152.

O'Reilly, J. E., Maritorena, S., Mitchell, B. G., Siegel, D. A., Carder, K. L., Garver, S. A., Kahru, M., and McClain, C. R. (1998), Ocean color chlorophyll algorithms for SeaWiFS, *J. Geophys. Res.*, *103*, 24937-24953.

O'Reilly, J. E., Maritorena, S., Siegel, D. A., O'Brien, M. C., Toole, D., Mitchell, B. G., Kahru, M., Chavez, F. P., Strutton, P., Cota, G. F., Hooker, S. B., McClain, C. R., Carder, K. L., Muller-Karger, F., Harding, L., Magnuson, A., Phinney, D., Moore, G. F., Aiken, J., Arrigo, K. R., Letelier, R., and Culver, M. (2000), Ocean Colr Chlorophyll a Algorithms for SeaWiFS, OC2 and OC4: Version 4, SeaWiFS Postlaunch Technical Report Series,NASA Tech. Memo. 2000-206892, p8-22, S.B. Hooker and E.R. Firestone, Eds., NASA Goddard Space Flight Center, Greenbelt, Maryland.

Platt, T., Sathyendranath, S., Caverhill, C., and Lewis, M. (1988), Ocean primary production and available light: Further algorithms for remote sensing, *Deep-Sea Research Part I*, *35*, 855-879.

Ramachandran, S., and Wang, M. (2011), Near-real-time ocean color data processing using ancillary data from the Global Forecast System model, *IEEE Trans. Geosci. Remote Sens.*, *49*, 1485-1495, doi:10.1109/TGRS.2010.2078825.

Ruddick, K. G., Ovidio, F., and Rijkeboer, M. (2000), Atmospheric correction of SeaWiFS imagery for turbid coastal and inland waters, *Appl. Opt.*, *39*, 897-912.

Salomonson, V. V., Barnes, W. L., Maymon, P. W., Montgomery, H. E., and Ostrow, H. (1989), MODIS: advanced facility instrument for studies of the Earth as a system, *IEEE Trans. Geosci. Remote Sensing*, *27*, 145-152.

Sathyendranath, S., Gouveia, A. D., Shetye, S., Ravindran, P., and Platt, T. (1991), Biological control of surface temperature in the Arabian Sea, *Nature*, *349*, 54-56.

Sathyendranath, S., Platt, T., Caverhill, C. M., Warnock, R., and Lewis, M. (1989), Remote sensing of oceanic primary production: Computations using a spectral model, *Deep-Sea Research*, *36*, 431-453.

Shettle, E. P., and Fenn, R. W. (1979), Models for the Aerosols of the Lower Atmosphere and the Effects of Humidity Variations on Their Optical Properties,AFGL-TR-79-0214, p1-94, U.S. Air Force Geophysics Laboratory, Hanscom Air Force Base, Mass.

Shi, W., and Wang, M. (2007a), Observations of a Hurricane Katrina-induced phytoplankton bloom in the Gulf of Mexico, *Geophy. Res. Lett.*, *34*, L11607, doi:10.1029/2007GL029724.

Shi, W., and Wang, M. (2007b), Detection of turbid waters and absorbing aerosols for the MODIS ocean color data processing, *Remote Sens. Environ.*, *110*, 149-161.

Shi, W., and Wang, M. (2008), Three-dimensional observations from MODIS and CALIPSO for ocean responses to cyclone Nargis in the Gulf of Martaban, *Geophy. Res. Lett.*, *35*, L21603, doi:10.1029/2008GL035279.

Shi, W., and Wang, M. (2009a), Satellite observations of flood-driven Mississippi River plume in the spring of 2008, *Geophy. Res. Lett.*, *36*, L07607, doi:10.1029/2009GL037210.

Shi, W., and Wang, M. (2009b), Green macroalgae blooms in the Yellow Sea during the spring and summer of 2008, *J. Geophys. Res.*, *114*, C12010, doi:10.1029/2009JC005513.

Shi, W., and Wang, M. (2009c), An assessment of the black ocean pixel assumption for MODIS SWIR bands, *Remote Sens. Environ.*, *113*, 1587-1597.

Shi, W., and Wang, M. (2010a), Characterization of global ocean turbidity from Moderate Resolution Imaging Spectroradiometer ocean color observations, *J. Geophys. Res.*, *115*, C11022, doi:10.1029/2010JC006160.

Shi, W., and Wang, M. (2010b), Satellite observations of the seasonal sediment plume in central East China Sea, *J. Marine Systems*, *82*, 280-285, doi:10.1016/j.jmarsys.2010.06.002.

Shi, W., and Wang, M. (2012a), Sea ice properties in the Bohai Sea measured by MODIS-Aqua: 1. Satellite algorithm development, *J. Marine Systems*, (In press).

Shi, W., and Wang, M. (2012b), Sea ice properties in the Bohai Sea measured by MODIS-Aqua: 2. Study of sea ice seasonal and interannual variability, *J. Marine Systems*, (In press).

Shi, W., Wang, M., and Jiang, L. (2011a), Spring-neap tidal effects on satellite ocean color observations in the Bohai Sea, Yellow Sea, and East China Sea, *J. Geophys. Res.*, *116*, C12032, doi:10.1029/2010JC007234.

Shi, W., Wang, M., Li, X., and Pichel, W. G. (2011b), Ocean sand ridge signatures in the Bohai Sea observed by satellite ocean color and synthetic aperture radar measurements, *Remote Sens. Environ.*, *115*, 1926-1934, doi: 10.1016/j.rse.2011.03.015.

Siegel, D. A., Doney, S. C., and Yoder, J. A. (2002), The North Atlantic spring phytoplankton bloom and sverdrup's critical depth hypothesis, *Science*, *296*, 730-733.

Siegel, D. A., Wang, M., Maritorena, S., and Robinson, W. (2000), Atmospheric correction of satellite ocean color imagery: the black pixel assumption, *Appl. Opt., 39*, 3582-3591.

Son, S., and Wang, M. (2009), Environmental responses to a land reclamation project in South Korea, *Eos Trans. AGU, 90*, 398-399.

Son, S., Wang, M., and Shon, J. (2011), Satellite observations of optical and biological properties in the Korean dump site of the Yellow Sea, *Remote Sens. Environ., 115*, 562-572, doi: 10.1016/j.rse.2010.10.002.

Stumpf, R. P., Arnone, R. A., Gould, R. W., Martinolich, P. M., and Ransibrahmanakul, V. (2003), A partially coupled ocean-atmosphere model for retrieval of water-leaving radiance from SeaWiFS in coastal waters, SeaWiFS Postlaunch Technical Report Series,Vol. 22, NASA Tech. Memo. 2003-206892, S. B. Hooker and E. R. Firestone, Eds., p51-59, NASA Goddard Space Flight Center, Greenbelt, Maryland.

Wang, M. (1999a), A sensitivity study of SeaWiFS atmospheric correction algorithm: Effects of spectral band variations, *Remote Sens. Environ., 67*, 348-359.

Wang, M. (1999b), Atmospheric correction of ocean color sensors: Computing atmospheric diffuse transmittance, *Appl. Opt., 38*, 451-455.

Wang, M. (2002), The Rayleigh lookup tables for the SeaWiFS data processing: Accounting for the effects of ocean surface roughness, *Int. J. Remote Sens., 23*, 2693-2702.

Wang, M. (2004), Extrapolation of the aerosol reflectance from the near-infrared to the visible: the single-scattering epsilon vs multiple-scattering epsilon method, *Int. J. Remote Sens., 25*, 3637-3650.

Wang, M. (2005), A refinement for the Rayleigh radiance computation with variation of the atmospheric pressure, *Int. J. Remote Sens., 26*, 5651-5663.

Wang, M. (2006), Aerosol polarization effects on atmospheric correction and aerosol retrievals in ocean color remote sensing, *Appl. Opt., 45*, 8951-8963.

Wang, M. (2007), Remote sensing of the ocean contributions from ultraviolet to near-infrared using the shortwave infrared bands: simulations, *Appl. Opt., 46*, 1535-1547.

Wang, M., and Bailey, S. (2001), Correction of the sun glint contamination on the SeaWiFS ocean and atmosphere products, *Appl. Opt., 40*, 4790-4798.

Wang, M., and Gordon, H. R. (1994), A simple, moderately accurate, atmospheric correction algorithm for SeaWiFS, *Remote Sens. Environ., 50*, 231-239.

Wang, M., and Shi, W. (2005), Estimation of ocean contribution at the MODIS near-infrared wavelengths along the east coast of the U.S.: Two case studies, *Geophy. Res. Lett., 32*, L13606, doi:10.1029/2005GL022917.

Wang, M., and Shi, W. (2007), The NIR-SWIR combined atmospheric correction approach for MODIS ocean color data processing, *Opt. Express, 15*, 15722-15733.

Wang, M., and Shi, W. (2008), Satellite observed algae blooms in China's Lake Taihu, *Eos Trans. AGU, 89*, 201-202, doi:10.1029/2008EO220001.

Wang, M., and Shi, W. (2012), Sensor noise effects of the SWIR bands on MODIS-derived ocean color products, *IEEE Trans. Geosci. Remote Sens.*, (In press).

Wang, M., Shi, W., and Tang, J. (2011), Water property monitoring and assessment for China's inland Lake Taihu from MODIS-Aqua measurements, *Remote Sens. Environ.*, *115*, 841-854, doi:10.1016/j.rse.2010.11.012.

Wang, M., Son, S., and L. W. Harding, J. (2009a), Retrieval of diffuse attenuation coefficient in the Chesapeake Bay and turbid ocean regions for satellite ocean color applications, *J. Geophys. Res.*, *114*, C10011, doi: 10.1029/2009JC005286.

Wang, M., Son, S., and Shi, W. (2009b), Evaluation of MODIS SWIR and NIR-SWIR atmospheric correction algorithm using SeaBASS data, *Remote Sens. Environ.*, *113*, 635-644.

Wang, M., Tang, J., and Shi, W. (2007), MODIS-derived ocean color products along the China east coastal region, *Geophy. Res. Lett.*, *34*, L06611, doi:10.1029/2006GL028599.

Werdell, P. J., Franz, B. A., and Bailey, S. W. (2010), Evaluation of shortwave infrared atmospheric correction for ocean color remote sensing of Chesapeake Bay, *Remote Sens. Environ.*, *114*, 2238-2247, doi: 10.1016/j.rse.2010.04.027.

Wu, Y., Tang, C., Sathyendranath, S., and Platt, T. (2007), The impact of bio-optical heating on the properties of the upper ocean: A sensitivity study using a 3-D circulation model for the Labrador Sea, *Deep-Sea Research Part II*, *54*, 2630-2642.

Yang, H., and Gordon, H. R. (1997), Remote sensing of ocean color: assessment of water-leaving radiance bidirectional effects on atmospheric diffuse transmittance, *Appl. Opt.*, *36*, 7887-7897.

Zhang, H., and Wang, M. (2010), Evaluation of sun glint models using MODIS measurements, *J. Quant. Spectrosc. Radiat. Transfer*, *111*, 492-506.

END OF DOCUMENT